J. Fluid Mech. (2010), *vol.* 655, *pp.* 38–71.
doi:10.1017/S0022112010000704

Non-equilibrium effects in capillarity and interfacial area in two-phase flow: dynamic pore-network modelling

V. JOEKAR-NIASAR[1]†, S. M. HASSANIZADEH[1] AND H. K. DAHLE[2]

[1]Department of Earth Sciences, Utrecht University, PO Box 80021, 3508 TA Utrecht, The Netherlands

[2]Department of Mathematics, University of Bergen, Johannes Brunsgate 12, N-5007 Bergen, Norway

(Received 13 August 2009; revised 2 February 2010; accepted 2 February 2010)

Current macroscopic theories of two-phase flow in porous media are based on the extended Darcy's law and an algebraic relationship between capillary pressure and saturation. Both of these equations have been challenged in recent years, primarily based on theoretical works using a thermodynamic approach, which have led to new governing equations for two-phase flow in porous media. In these equations, new terms appear related to the fluid–fluid interfacial area and non-equilibrium capillarity effects. Although there has been a growing number of experimental works aimed at investigating the new equations, a full study of their significance has been difficult as some quantities are hard to measure and experiments are costly and time-consuming. In this regard, pore-scale computational tools can play a valuable role. In this paper, we develop a new dynamic pore-network simulator for two-phase flow in porous media, called DYPOSIT. Using this tool, we investigate macroscopic relationships among average capillary pressure, average phase pressures, saturation and specific interfacial area. We provide evidence that at macroscale, average capillary pressure–saturation–interfacial area points fall on a single surface regardless of flow conditions and fluid properties. We demonstrate that the traditional capillary pressure–saturation relationship is not valid under dynamic conditions, as predicted by the theory. Instead, one has to employ the non-equilibrium capillary theory, according to which the fluids pressure difference is a function of the time rate of saturation change. We study the behaviour of non-equilibrium capillarity coefficient, specific interfacial area, and its production rate versus saturation and viscosity ratio.

A major feature of our pore-network model is a new computational algorithm, which considers capillary diffusion. Pressure field is calculated for each fluid separately, and saturation is computed in a semi-implicit way. This provides more numerical stability, compared with previous models, especially for unfavourable viscosity ratios and small capillary number values.

1. Introduction

1.1. *Theories of two-phase flow including interfacial area*

Understanding the physics of multiphase flow in porous media is important in many fields such as hydrogeology, reservoir engineering, biomechanical engineering, fuel

† Email address for correspondence: joekar@geo.uu.nl

cells, and other industrial applications. Current theories of multiphase flow are based on Darcy's law, which assumes that the only driving forces for flow of each fluid are the gravity and the gradient in fluid pressure. The resisting force is assumed to be linearly proportional to the relative fluid velocity with respect to the solid. This results in a linear relationship between the flow velocity and driving forces. While these assumptions are reasonable for single-phase flow, one may expect many other factors to affect the balance of forces in the case of multiphase flow. Among these are interfacial forces that govern the distribution of interfaces in the porous medium. In fact, through the application of rational thermodynamics, Hassanizadeh & Gray (1990, 1993*a*) developed a theory of two-phase flow in which interfacial areas were introduced as separate thermodynamic entities, possessing mass, momentum and energy. They derived momentum balance equations not only for phases but also for interfaces, and macroscale effects of interfacial forces were explicitly included. They derived the following extended form of Darcy's law in which gradients of saturations and specific interfacial area appeared as driving forces:

$$\boldsymbol{v}^{\alpha,s} = -\boldsymbol{K}^{\alpha} \cdot (\nabla P^{\alpha} - \rho^{\alpha} \boldsymbol{g} - \Omega^{\alpha a} \nabla a^{nw} - \Omega^{\alpha S} \nabla S^{\alpha})/\mu^{\alpha}, \quad \alpha = w, n, \tag{1.1}$$

where $\boldsymbol{K}^{\alpha}$ is an α-phase permeability tensor, $\Omega^{\alpha a}$ and $\Omega^{\alpha S}$ represent material properties, $\boldsymbol{v}^{\alpha,s}$ denotes relative velocity of fluid phase α with respect to the solid, $\boldsymbol{g}$ is gravity vector, a^{nw} is the specific area of fluid–fluid interfaces (amount of interfacial area per unit volume of the porous medium) and P^{α}, ρ^{α}, S^{α}, and μ^{α} are pressure, mass density, saturation and viscosity of the α-phase. The superscripts w and n designate wetting and non-wetting phases, respectively. Hassanizadeh & Gray (1990, 1993*a*) also obtained the following equation for the average velocity of fluid–fluid interfaces:

$$\boldsymbol{w}^{nw,s} = -\boldsymbol{K}^{nw} \cdot [\nabla (a^{nw} \sigma^{nw}) + \Omega^{nw} \nabla S^{w}], \tag{1.2}$$

where $\boldsymbol{K}^{nw}$ is a permeability tensor for nw-interfaces, Ω^{nw} represents a material property, $\boldsymbol{w}^{nw,s}$ denotes the relative macroscopic velocity of fluid–fluid interfaces with respect to the solid, and σ^{nw} is the macro-scale interfacial tension. These equations may be seen as the truly extended forms of Darcy's law, not only for a phase but also for an interface. They must be supplemented with the following equations of balance of volume for phase saturations and specific interfacial area (assuming incompressible phases and constant mass density for interfaces):

$$\varphi \frac{\partial S^{\alpha}}{\partial t} + \nabla \cdot \boldsymbol{v}^{\alpha} = 0, \quad \alpha = w, n, \tag{1.3}$$

$$\frac{\partial a^{nw}}{\partial t} + \nabla \cdot (a^{nw} \boldsymbol{w}^{nw}) = E^{nw}, \tag{1.4}$$

where φ is porosity, $\boldsymbol{v}^{\alpha}$ and $\boldsymbol{w}^{nw}$ denote average velocities of α-phase and nw-interfaces, respectively, and E^{nw} is the net rate of production of nw-interfaces. It is proposed that E^{nw} should depend on saturation and its time rate of change. However, so far there has been no study of this dependence.

Another central equation in theories of two-phase flow is the so-called capillary pressure–saturation relationship, which is commonly written as

$$P^{n} - P^{w} = P^{c}(S^{w}). \tag{1.5}$$

In fact, there are two major assumptions in this equation: capillary pressure is a function of wetting phase saturation only, and fluids pressure difference is equal to capillary pressure (at all times and under all conditions). Regarding the first assumption, it is known that the capillary pressure–saturation relationship is not

unique and, even though it is obtained under equilibrium conditions, it is a function of the history of fluids movements. In fact, it depends not only on the volume fraction of each phase but also on their microscale distribution. Therefore, one would expect capillary pressure to depend also on the interfacial curvature and/or specific interfacial area. Hassanizadeh & Gray (1993*b*) have suggested that the non-uniqueness in the capillary pressure–saturation relationship is indeed due to the absence of specific interfacial area, and they proposed the following equation for capillary pressure:

$$P^c(S^w) = P^c(S^w, a^{nw}). \tag{1.6}$$

A number of computational and experimental works have shown that under a wide range of drainage and imbibition histories, P^c–S^w–a^{nw} surfaces more or less coincide. This means that inclusion of a^{nw} leads to the removal or significant reduction of hysteresis in capillary pressure versus saturation relationship. In other words, a unique P^c–S^w–a^{nw} surface may exist (e.g. Reeves & Celia 1996; Cheng, Pyrak-Nolte & Nolte 2004; Joekar-Niasar, Hassanizadeh & Leijnse 2008; Joekar-Niasar *et al.* 2009, 2010; Porter, Schaap & Wildenschild 2009).

Regarding the second assumption underlying (1.5), it is now an established fact that $P^n - P^w$ is equal to capillary pressure but only under equilibrium conditions (see Hassanizadeh, Celia & Dahle 2002 for an extended review of experimental evidences). For non-equilibrium situations, the following equation for the difference in fluid pressures has been suggested (Stauffer 1978; Kalaydjian & Marle 1987; Hassanizadeh & Gray 1990):

$$P^n - P^w = P^c - \tau \frac{\partial S^w}{\partial t}, \tag{1.7}$$

where τ, a non-equilibrium capillarity coefficient, is a material property that may still be a function of saturation.

Recently, Niessner & Hassanizadeh (2008) have set up a numerical model based on (1.1)–(1.4), (1.6) and (1.7). They have shown that the extended model can properly capture physical processes such as capillary hysteresis. However, much needs to be done for finding ways of studying various terms in these equations and gaining insight in the interplay of various effects.

1.2. *Dynamic pore-network models for two-phase flow*

Pore-network models can be divided into quasi-static and dynamic ones. Quasi-static pore-network models, which have been used extensively, simulate only equilibrium states of drainage and imbibition processes without solving the pressure field (see e.g. Fatt 1956; Reeves & Celia 1996; Held & Celia 2001; Blunt *et al.* 2002; Valvatne & Blunt 2004; Joekar-Niasar *et al.* 2008, 2009). However, the dynamic pore-network model can simulate transient behaviour of flow with time.

Among different computational methods for simulating transient behaviour of two-phase flow in porous media, dynamic pore-network modelling has been extensively used as an upscaling tool, as it is relatively simple and computationally less demanding than the other computational methods. For example, the lattice Boltzmann (LB) method, which solves the Navier–Stokes equation, is computationally too expensive and memory-demanding compared with dynamic pore-network models, which usually solve a simplified form of the momentum equation such as Stokes equation. For instance, Porter *et al.* (2009) have recently used the LB method to simulate air–water flow in glass beads with physical domain size of less than 500 pores, which was discretized into $207 \times 207 \times 166$ voxels. At a flux of 0.00008 mu ts^{-1} (mass unit per time

step), approximately 50 000 ts were required to obtain only a 5 % change in saturation, which took about 1.25 days to run on four AMD64 CPU (2.8 GHz) machines in parallel. Roughly speaking, for their given specifications of domain and fluids, a full drainage simulation would take more than 100 days with a single processor. In another study, Pan, Hilpert & Miller (2004) have stated that computational limitations are of great concern when applying LB simulations for multiphase porous medium systems, even using large-scale parallel computing. They could not afford to simulate domains with sizes close to a representative elementary volume (REV). The advantage of the LB method, however, is that it can solve equations in an arbitrary pore space geometry and topology without simplification. However, in pore-network modelling, the porous medium should be idealized to some simple geometries so that essential features are adequately represented (Celia, Reeves & Ferrand 1995). This idealization can lead to loss of geometrical and topological information. Also, information on temporal changes within a single pore in pore-network models is not as detailed as in LB simulations. Nevertheless, simplifications in pore-network modelling allow us to simulate much larger domains and with much less computational effort; this is a major advantage.

The first dynamic pore-network model reported in the literature was developed by Koplik & Lasseter (1985), who simulated dynamics of two-phase imbibition process in a two-dimensional unstructured pore-network model with circular cross-sections. Later, several dynamic pore-network models were developed for various applications, such as simulating two-phase drainage (see e.g. Aker *et al.* 1998*a*; Dahle & Celia 1999; Nordhaug, Celia & Dahle 2003; Al-Gharbi & Blunt 2005; Gielen *et al.* 2005), imbibition (see e.g. Koplik & Lasseter 1985; Hughes & Blunt 2000; Thompson 2002), evaporation (e.g. Prat 2002), three-phase flow (see e.g. Pereira *et al.* 1996) and ganglia movement (see e.g. Dias & Payatakes 1986*a*,*b*; Constantinides & Payatakes 1996). Of notable significance have been the models developed by *Payatakes* and co-workers (see e.g. Dias & Payatakes 1986*a*,*b*; Constantinides & Payatakes 1996), which can simulate ganglia displacement.

Dynamics of two-phase flow during drainage have been studied in several works. Aker *et al.* (1998*a*), Aker, Maloy & Hansen (1998*b*) and Van der Marck, Matsuura & Glas (1997) studied pressure field evolution with time for a range of viscosity ratios and capillary numbers during drainage. Capillary number (C_a) is traditionally defined as the ratio of viscous forces of the invading phase to capillary forces ($(\mu_{inv} q_{inv})/\sigma^{nw}$) and the viscosity ratio is the ratio of viscosity of invading fluid to that of the receding fluid. Dahle & Celia (1999) developed an IMPES-type (implicit pressure, explicit saturation) algorithm to explicitly model the dynamics of fluid–fluid interfaces and also pressure field evolution with time for favourable viscosity ratios. Singh & Mohanty (2003) as well as Al-Gharbi & Blunt (2005) studied the effect of capillary number on residual water saturation during drainage for constant injection rate at the boundaries. They also investigated the fractional flow behaviour for different flow rates as did Knudsen & Hansen (2002) and Knudsen, Aker & Hansen (2002). Mogensen & Stenby (1998) developed an angular-shape pore-network model to study dynamics of imbibition under the effect of flow rate, viscosity ratio, aspect ratio and coordination number.

Thompson (2002) developed a dynamic pore-network model to investigate imbibition process in fibrous material for water–air system (favourable viscosity ratio). He solved pressure fields for each phase separately, including local capillary pressure. However, his model failed to simulate capillary-dominated conditions. Payatakes and co-workers studied dynamics of oil ganglia as well as dependency

of relative permeabilities curves on the capillary number and viscosity ratio in several publications (Payatakes 1982; Dias & Payatakes 1986*a*,*b*; Constantinides & Payatakes 1991, 1996). Nguyen *et al.* (2006) employed a dynamic pore-network model to study the effect of flow rate on snap-off during imbibition. They also showed dependency of relative permeability on flow rate as did Avraam & Payatakes (1995*a*).

1.3. *Features and objectives*

The focus of this work is twofold. The major goal is to investigate theories for two-phase flow in porous media including interfacial area and the side goal is to present a new numerical algorithm for two-phase dynamic pore-network modelling.

1.3.1. *Investigation of theories for two-phase flow*

In the extended theories of two-phase flow in porous media, there are new variables and parameters, which are experimentally difficult to be investigated. Major objectives of this work are as follows: (i) investigation of uniqueness of (1.6) under equilibrium and non-equilibrium conditions during drainage; (ii) investigation of the validity of (1.7); (iii) proposing an explicit formula for the dependence of the interfacial area production term (in (1.4)) on saturation and its time rate of change.

Hassanizadeh & Gray (1993*b*) state that the P^c–S^w–a^{nw} relationship is supposed to be an intrinsic property of the fluids–solid system and valid under all thermodynamic conditions. The latter issue has not yet been investigated as all measurements of the P^c–S^w–a^{nw} relationship have been carried out under equilibrium conditions. So, one goal of this paper is to determine specific interfacial area, average capillary pressure, and saturation under various dynamic conditions as well as quasi-equilibrium situation, albeit for drainage only, and determine whether all data points fall on a single a^{nw}–P^c–S^w surface.

Equation (1.7) has been the subject of many studies in recent years, both computationally (see e.g. Dahle, Celia & Hassanizadeh 2005; Gielen *et al.* 2005; Manthey, Hassanizadeh & Helmig 2005; Das, Mirzaei & Widdows 2006) and experimentally (see e.g. Hassanizadeh, Oung & Manthey 2004; Oung, Hassanizadeh & Bezuijen 2005; O'Carroll, Phelan & Abriola 2005). Nevertheless, there are still open questions regarding the dependency of τ on various factors. In this paper, we investigate the dependency of τ on saturation as well as fluids viscosity ratio.

Regarding (1.4), although there has been considerable progress in recent years in finding ways of measuring specific interfacial area (see e.g. Brusseau, Popovicova & Silva 1997; Costanza-Robinson & Brusseau 2002; Cheng *et al.* 2004; Culligan *et al.* 2004, 2006; Chen & Kibbey 2006; Brusseau *et al.* 2006; Chen *et al.* 2007), there is as yet no experimental (or computational) study of the interface production term. One of the goals of this paper is to study the dynamics of fluid–fluid interfaces and to provide insight into the dependence of this production term on other primary variables. In particular, the dependence of E^{nw} on saturation and its time rate of change and viscosity ratio will be studied. This term is very important because it prescribes the appearance and disappearance of interfaces as the two-phase flow occurs.

1.3.2. *Computational improvement of two-phase dynamic pore-network modelling*

Despite the fact that numerous dynamic pore-network models have been proposed over the years, the quasi-static models have remained dominant, largely because of computational tractability. In particular, the strong nonlinearity at the pore scale causes severe stability problemsin dynamic pore-network models. In this paper, we

propose a computational algorithm, which is different from the previous dynamic pore-network models, in the following respects.

(*a*) Similar to Thompson (2002), and in contrast to all other dynamic pore-network models, we assign a separate pressure field to each phase within both pore bodies and pore throats, and include local capillary pressures in pore bodies. We include a snap-off criterion to account for the effect of pore geometry on flow.

(*b*) The computational algorithm for saturation update is improved in order to have numerical stability in simulations even for a capillary-dominated flow. A semi-implicit approach is used in the saturation update. Thus, the resulting set of equations for fluid pressures contain both advection-type terms (corresponding to viscous forces) and diffusion-type terms (corresponding to capillary forces). This gives more versatility to our formulation so that competition between viscous forces and capillary forces is properly modelled. We will show that in contrast to previous studies (see e.g. Thompson 2002; Al-Gharbi & Blunt 2005), we can obtain full consistency between fluid occupancy at equilibrium resulting from quasi-static simulations and dynamic simulations for the same boundary conditions.

(*c*) We significantly improve computational efficiency in pressure field calculations. Using total pressure definition (phase pressures weighted with saturation), calculation of phase pressures is done in a cheaper way compared with previous dynamic pore-network models. In addition, the model has been tested for both favourable and unfavourable viscosity ratios, which is numerically stable.

(*d*) Tracking fluid–fluid interfaces in pore throats is computationally expensive. Allocating zero filling time for pore throats allows us to model a much larger domain. On the other hand, we consider infinite conductance (zero flow resistance) in pore bodies.

2. Classification of dynamic pore-network models

Dynamic pore-network models differ among themselves in three main features: network structure, geometry of the elements, and computational algorithm for solving the pressure field. A brief description of these features in various dynamic pore-network models developed so far is given in this section.

2.1. *Network structure*

The network structure is characterized by the positioning of nodes and the number and orientation of links. If the nodes are positioned at the vertices of a regular lattice, the network is referred to as a 'structured' one, and otherwise it is 'unstructured'. If all nodes have the same number of links connected, the networked is 'isotropic', and otherwise it is 'anisotropic'. Dynamic pore-network models developed to date are mostly structured and isotropic. However there are some cases that are structured and anisotropic (e.g. Mogensen & Stenby 1998), unstructured and isotropic (e.g. King 1987; Blunt & King 1991), and unstructured and anisotropic (e.g. Koplik & Lasseter 1985; Thompson 2002).

2.2. *Geometry of the elements*

Conventional pore-network models consist of pore bodies, which are connected to each other by pore throats. The geometry of pore-network models can be studied based on two different aspects of these network elements: volumes and cross-sectional shapes assigned to them.

2.2.1. *Volumes assigned to elements*

In this regard, there are three different types of network models as described below.

(i) Pore bodies have volume but no resistance; pore throats have negligible volume but offer resistance to flow. This assumption will help to save computation time and memory in simulations, since it is not necessary to track interfaces within pore throats. Also, pressure drop within pore bodies can be neglected so that a single pressure value can be assigned to (each fluid within) a pore body. Examples are the works by Blunt & King (1990) and Gielen *et al.* (2005).

(ii) Both pore bodies and pore throats have volume and resistance. Almost none of the dynamic pore-network models reported in the literature correspond to this case. The only exceptions to our knowledge are Mogensen & Stenby (1998) and Singh & Mohanty (2003). However, they have not shown gains of their models compared with previous ones.

(iii) A pore body and a pore throat are combined into one element that has both volume and resistance. Combined pore throat–pore body elements may have a varying cross-section. No specific properties, such as volume and resistance, are assigned to the connection points. This structure has been used in pore-network models of Payatakes and co-workers (see e.g. Dias & Payatakes 1986*a*,*b*; Valvanides, Constantinides & Payatakes 1998) as well as in works by Aker *et al.* (1998*a*,*b*), Dahle & Celia (1999), Knudsen & Hansen (2002), Knudsen *et al.* (2002) and Al-Gharbi & Blunt (2005), among others.

2.2.2. *Geometry of elements, cross-section*

The geometry chosen for pore bodies and pore throats has consequences for the computational algorithm. Because of the significant simplicity of circular cross-sections, most dynamic network models have a circular cross-section. However, there are a few models with angular cross-sections. Valvanides *et al.* (1998) and Al-Gharbi & Blunt (2005) have assumed triangular cross-sections, whereas Mogensen & Stenby (1998), Hughes & Blunt (2000), Singh & Mohanty (2003) and Gielen *et al.* (2005) have assumed cubic pore bodies and parallelepiped pore throats. Pereira *et al.* (1996), Van der Marck *et al.* (1997) and Thompson (2002) have also considered other angular cross-sections. The main reason for using angular cross-sections is to allow existence of corner flow along edges of a pore element. In angular cross-sections, it is possible to have two fluids simultaneously present at any given cross-section, with the wetting phase filling the corners.

2.3. *Computational algorithms*

There are two general algorithms for solving the pressure field in a dynamic pore-network model: single-pressure and two-pressure algorithms. These are explained in detail in the following.

2.3.1. *Single-pressure algorithm*

In this algorithm, regardless of the occupancy of pore bodies, a single pressure is assigned to each pore body. This single-pressure algorithm is generally applied in the following three different approaches.

(i) It is assumed that each pore body or pore throat is occupied by one fluid only at a time. This is generally applied to networks with circular cross-sections (e.g. Van der Marck *et al.* 1997; Aker *et al.* 1998*a*,*b*).

(ii) It is assumed that both fluids can be present within a pore body but not within a pore throat. Then, it is assumed that the local capillary pressure is negligible. Therefore, to each pore element a single pressure is assigned (e.g. Gielen *et al.* 2005).

(iii) It is assumed that an equivalent fluid can be defined as having a single pressure. Thus, pore bodies and pore throats are filled with the equivalent fluid and an equivalent conductivity is assigned to each pore throat (e.g. Mogensen & Stenby 1998; Al-Gharbi & Blunt 2005).

In all three approaches, the following volume balance equation for pore bodies is solved:

$$\sum_{j=1}^{N_i} Q_{ij} = 0, \tag{2.1}$$

where N_i is the number of pore throats connected to pore body i, and $Q_{ij}\left[L^3T^{-1}\right]$ is the volumetric fluxes through pore throat ij. This flux is calculated by means of the Washburn equation (Washburn 1921):

$$Q_{ij} = K_{ij}^{eq}\left(\Delta p_{ij} - p_{ij}^{c}\right), \tag{2.2}$$

$$\Delta p_{ij} = p_i - p_j, \tag{2.3}$$

where $K_{ij}^{eq}[M^{-1}L^4T]$ is an equivalent conductivity, which is a function of the pore throat radius, pore throat length, fluid viscosities and location of the meniscus in the pore throat; and $p_{ij}^{c}[ML^{-1}T^{-2}]$ is the effective capillary pressure (depending on the number of interfaces located) between pore bodies i and j.

Obviously, corner flow is not included in Washburn's formulation. Nevertheless, (2.2) has been modified and used for angular cross-sections, using the concept of equivalent phase (see approach (iii) above). It is assumed that a pore throat is filled simultaneously by two fluids, each fluid having its own conductivity. In the pore bodies on the two sides of a pore throat, each phase has its own pressure, which drives the flow. However, to simplify the problem and decrease computational effort, a single (virtual) pressure is assigned to the two fluids in pore bodies. Equation (2.1) is then applied to calculate the flow. It is assumed that a pore throat is filled with a single fluid with the equivalent conductivity K_{ij}^{eq}. This is achieved by averaging conductivities of phases using the rule of equivalent resistor for electrical resistor circuits. So, instead of solving for two pressure fields, one can solve for a single pressure field (see e.g. Mogensen & Stenby 1998; Al-Gharbi & Blunt 2005; Bravo, Araujo & Lago 2007).

The advantage of the single-pressure approach is that it simplifies the problem and reduces computational effort. However, it also has some disadvantages. For example, no local capillary pressure for pore bodies can be defined. This means that no information from the interface behaviour under dynamic conditions can be gained using this type of dynamic pore-network models. Moreover, this approach exhibits some inconsistent behaviours in fluids occupancy in the network. In particular, snapshots of fluid occupancy obtained from quasi-static and dynamic pore-network models, for the same boundary conditions, are not the same. If we do not assign any dynamics to the contact angle, we would expect to obtain the same equilibrium fluid occupancy resulting from quasi-static pore-network model as from a dynamic pore-network model for the same boundary conditions. However, Al-Gharbi & Blunt (2005) showed that employing the concept of equivalent phase pressure solver induced an inconsistent behaviour in fluid occupancy in their dynamic pore-network model.

2.3.2. *Two-pressure algorithm*

In this algorithm, when a pore body is filled with two fluids, each fluid is assumed to have its own pressure. To our knowledge, this concept was employed for the first time by Thompson (2002), who defined variable local capillary pressures in pore bodies and solved the pressure field for both phases separately. The local capillary pressure for pore body i is defined as

$$p_i^c = p_i^n - p_i^w = f\left(s_i^w\right). \tag{2.4}$$

A flux Q_{ij}^{α} is assigned in a pore throat ij for each phase separately. Then, (2.1) is replaced by the following total volume balance for pore i:

$$\sum_{j=1}^{N_i} \left(Q_{ij}^n + Q_{ij}^w\right) = 0. \tag{2.5}$$

Moreover, a separate volume balance for each phase in a pore body is employed:

$$V_i \frac{\Delta s_i^{\alpha}}{\Delta t} = -\sum_{j=1}^{N_i} Q_{ij}^{\alpha}, \quad \alpha = w, n, \tag{2.6}$$

where V_i is the volume of pore body i, s_i^{α} is the saturation of phase α in pore body i, and Q_{ij}^{α} is the volumetric flux of phase α in pore body i, given by (2.7). The latter is given by an equation similar to the Washburn formula:

$$Q_{ij}^{\alpha} = -K_{ij}^{\alpha} \Delta p_{ij}^{\alpha}, \quad \alpha = w, n, \tag{2.7}$$

where K_{ij}^{α} is a function of geometry and fluid occupancy of pore throats. This formulation allows us to include mechanisms related to the local capillary pressure (such as snap-off, counter-current flow) in simulations.

3. Model description

In this paper, we employ the two-pressure algorithm. The procedure and results are described in detail below.

3.1. *Model features*

3.1.1. *Structure and geometry*

For predictive purposes, where pore-network models are used to simulate a specific porous medium, the network should be based on the real connectivity of pores (topology), aspect ratio (i.e. pore body radius divided by pore throat radius), and shape of pores (geometry). Because of the following reasons, the structure of network (coordination number) can be considered as a minor issue in this study. (*a*) We are interested in studying the qualitative behaviour of new theories of two-phase flow, and we prefer to eliminate effects of heterogeneities in our simulations. (*b*) Mogensen & Stenby (1998) studied effects of pores connectivity (coordination number) and aspect ratio using pore-network modelling. They found that with the increase of capillary number, the effect of variation of coordination number on dynamics of the system and residual saturation decreases. (*c*) For theoretical purposes, regular lattice with fixed coordination number has generally been used, which is computationally simpler than the irregular unstructured networks.

Our pore-network model has a three-dimensional regular lattice structure with fixed coordination number of six. Pore bodies have cubic shape and pore throats

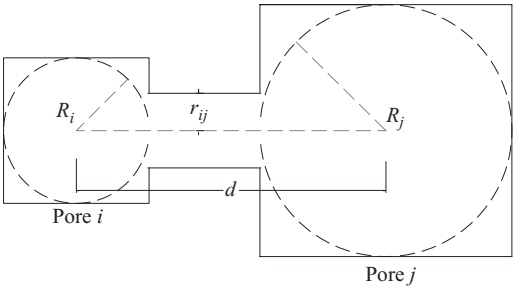

FIGURE 1. Geometrical configuration for determining the pore throat radius (r_{ij}) based on pore bodies radii R_i and R_j.

have square cross-sections. Figure 1 shows a schematic of two pore bodies and the connected pore throat. The size distribution of pore bodies is given by a truncated log-normal distribution, with no spatial correlation,

$$f(R_i;\sigma_{nd}) = \frac{\sqrt{2}\exp\left[-\frac{1}{2}\left(\ln\frac{R_i}{R_m}\Big/\sigma_{nd}\right)^2\right]}{\sqrt{\pi\sigma_{nd}^2}R_i\left[\operatorname{erf}\left(\ln\frac{R_{max}}{R_m}\Big/\sqrt{2\sigma_{nd}^2}\right)-\operatorname{erf}\left(\ln\frac{R_{min}}{R_m}\Big/\sqrt{2\sigma_{nd}^2}\right)\right]}, \tag{3.1}$$

where R_i is the radius of inscribed sphere in a pore body (so, the cube side length is $2R_i$), R_{min} is the lower range of truncation, R_{max} is the upper range of truncation, R_m is the mean of inscribed sphere radii, and σ_{nd} is the standard deviation. The radius and length of pore throats connecting the pore bodies are determined based on the size of neighbouring pore bodies. Spacings between the layers of the network in x-, y- and z-directions are chosen to be variable. Let the spacings between layers i and $i+1$ in the three directions be denoted by $\lambda_{x,i}$, $\lambda_{y,i}$ and $\lambda_{z,i}$. Then, designating each pore body by its lattice indices, namely i, j, and k, lattice spacings are defined as follows:

$$\lambda_{x,i} = \max\{R(i,j,k)+R(i+1,j,k) : j=1,n_y, k=1,n_z\}, \quad i=1,n_x, \tag{3.2a}$$
$$\lambda_{y,j} = \max\{R(i,j,k)+R(i,j+1,k) : i=1,n_x, k=1,n_z\}, \quad j=1,n_y, \tag{3.2b}$$
$$\lambda_{z,k} = \max\{R(i,j,k)+R(i,j,k+1) : i=1,n_x, j=1,n_y\}, \quad k=1,n_z, \tag{3.2c}$$

where n_x, n_y and n_z denote the number of pore bodies in the x-, y-, and z-directions, respectively. Then, the length of the pore throats is determined. On the basis of the length of a pore throat and sizes of its neighbouring pore bodies, the size of that pore throat cross-section is determined (for more detailed explanation refer to Joekar-Niasar *et al.* 2008). Consider two pore bodies i and j, with a centre-to-centre distance d (see figure 1), and inscribed pore radii R_i and R_j, respectively. We define the dimensionless $\widetilde{R_i}$ and $\widetilde{R_j}$ as follows:

$$\widetilde{R_i} = R_i/d, \qquad \widetilde{R_j} = R_j/d. \tag{3.3}$$

We can calculate dimensionless inscribed radius of the pore throat ij, $\widetilde{r_{ij}}$, as follows:

$$\widetilde{r_{ij}} = \varrho_i \varrho_j \left(\varrho_i^{1/n} + \varrho_j^{1/n}\right)^{-n}, \quad n > 0, \tag{3.4}$$

$$\varrho_i = \frac{\widetilde{R}_i \sin(\pi/4)}{(1 - \widetilde{R}_i \cos(\pi/4))^n}, \tag{3.5}$$

$$\varrho_j = \frac{\widetilde{R}_j \sin(\pi/4)}{(1 - \widetilde{R}_j \cos(\pi/4))^n}, \tag{3.6}$$

where n is a parameter which can control ratio between the radii of pore bodies and the pore throat. It should be larger than zero. Larger n results in smaller pore throats. In this work, we select $n = 0.1$ to have a significant overlapping between pore body and pore throat radii distributions. The resultant aspect ratio varies between (2.2) and (3.4).

3.1.2. *Boundary conditions*

It is assumed that the network is connected to a non-wetting phase reservoir on one side and a wetting phase reservoir on the other side. Dirichlet boundary conditions are imposed at these boundaries. We refer to the difference between the two boundary pressures as the global pressure difference P^c_{global}. After breakthrough of the pore throat ij at the lower boundary by the non-wetting fluid, we assign the same capillary pressure to both sides of the outlet pore throat, determined by the upstream pore body; $p^c_i = p^c_j$. Side boundary conditions are assumed to be periodic.

3.1.3. *Assumptions*

The following assumptions are imposed in the computational algorithm and network development.

(i) The volume of pore throats is negligible compared with the volume of pore bodies. Thus, the time required for filling a single pore throat is negligible compared with that of a pore body. Also, this volume is not included in the computation of network saturation.

(ii) Hydraulic resistance to flow in pore bodies is assumed to be negligible compared with that of pore throats.

(iii) Fluids are assumed immiscible and incompressible and the solid matrix is assumed to be rigid.

(iv) Flow in the pore throats is assumed to have low Reynolds number such that transient effects can be neglected at the pore scale. This allows us to use the Washburn equation for fluid fluxes through pores.

(v) No gravity effect has been considered in the simulations. Flow occurs because of the pressure difference across the boundaries. Adding gravity does not constitute any major complication in the code. But it does not affect results and conclusions.

3.1.4. *System parameters and specifications*

Tables 1 and 2 show the fluid properties and network specifications used in the simulations, respectively.

3.2. *Local rules*

3.2.1. *Capillary pressures for pore bodies and pore throats*

Since pore bodies in our model are cubic, the wetting phase always resides in the corners and along edges (see figure 10). The saturation of the pore body (i.e. volume of the wetting fluid divided by the volume of the pore body) depends on the prevailing

Specification	Symbol	Value	Unit
Contact angle	θ	0.0	deg.
Interfacial tension	σ^{nw}	0.0725	kg s^{-2}
Wetting fluid viscosity	μ^{w}	0.001	kg $m^{-1}s^{-1}$
Non-wetting fluid viscosity	μ^{n}	0.0001, 0.001, 0.01	kg $m^{-1}s^{-1}$

TABLE 1. Fluid properties in the simulations.

Specification	Symbol	Value	Unit
Lattice dimension		3D: $35 \times 35 \times 35$	–
(Two-dimensional only for figure 7)		2D: 70×70	
Lattice size		3D: $6 \times 6 \times 6$	mm^3
		2D: 12.5×12.5	mm^2
Minimum pore body inscribed radius	$R_{\min}$	0.0408	mm
Maximum. pore body inscribed radius	$R_{\max}$	0.234	mm
Mean pore body inscribed radius	R_m	0.114	mm
Standard deviation		0.169	mm

TABLE 2. Network parameters.

capillary pressure. For a given capillary pressure, curvature of the interface in the vertices and edges of the cube can be calculated and, consequently, the corresponding saturation can be estimated. In Appendix A, details of derivation of the (local) p_i^c–s_i^w relationship for a cubic pore body are presented. The resulting equation for p_i^c, in terms of the radius R_i of the inscribed sphere of the pore body i and the local wetting phase saturation, is:

$$p_i^c\left(s_i^w\right) = \frac{2\sigma^{nw}}{R_i\left(1-\exp\left(-6.83 s_i^w\right)\right)}. \tag{3.7}$$

A capillary pressure should also be assigned to a pore throat once it is invaded and both phases are present. We assume that capillary pressure in a pore throat is equal to the capillary pressure of the upstream pore body.

3.2.2. *Minimum wetting phase saturation in a pore body*

Obviously it is impossible to completely displace the wetting phase from the corners of a cube. We assume that each pore body has a minimum saturation $s_{i,min}^w$, which depends on the imposed global pressure difference (P_{global}^c defined in § 3.1.2) as well as the blockage of the invading fluid. The capillary blockage of invading fluid ($P_{e_{block}}^c$) is also a global variable defined to be the minimum entry capillary pressure of all pore throats that are connected to the non-wetting phase and not yet invaded. Thus, using the p_i^c–s_i^w relationship given by (3.7), the local minimum wetting phase saturation in a pore body may be determined as follows:

$$s_{i,min}^w = -\frac{1}{6.83}\ln\left(1-\frac{1}{R_i}\frac{2\sigma^{nw}}{\min\{P_{global}^c, P_{e_{block}}^c\}}\right). \tag{3.8}$$

3.2.3. *Entry capillary pressure for a pore throat*

We assume that a pore throat will be invaded by the non-wetting phase when the capillary pressure in a neighbouring pore body becomes larger than the entry capillary pressure of the pore throat. The latter can be calculated as follows (due to

Mayer & Stowe 1965; Princen 1969*a*,*b*, 1970; Ma, Mason & Morrow 1996):

$$p^c_{e,ij} = \frac{\sigma^{nw}}{r_{ij}} \left(\frac{\theta + \cos^2\theta - \pi/4 - \sin\theta\cos\theta}{\cos\theta - \sqrt{\pi/4 - \theta + \sin\theta\cos\theta}} \right), \tag{3.9}$$

where r_{ij} is the radius of inscribed circle of the pore throat cross-section, and θ is the contact angle.

3.2.4. *Conductivities of pore throats*

Conductivities of pore throats are determined based on the fluid occupancy and size of the pore throat. One of the following two different states may occur during drainage.

(*a*) The pore throat is occupied by the wetting phase only. For this case, the following equation was obtained by Azzam & Dullien (1977):

$$\left.\begin{aligned} K^w_{ij} &= \frac{\pi}{8\mu^w l_{ij}} \left(r^{eff}_{ij}\right)^4, \\ K^n_{ij} &= 0, \end{aligned}\right\} \tag{3.10}$$

where μ^w is the viscosity of the wetting phase, l_{ij} is the length of the pore throat, and

$$r^{eff}_{ij} = \sqrt{\frac{4}{\pi}} r_{ij}. \tag{3.11}$$

(*b*) The pore throat is invaded by the non-wetting phase, thus both phases may be flowing. Then, following Ransohoff & Radke (1988) we can write

$$K^w_{ij} = \frac{4 - \pi}{\beta\mu^w l_{ij}} \left(r^c_{ij}\right)^4, \tag{3.12}$$

$$K^n_{ij} = \frac{\pi}{8\mu^n l_{ij}} \left(r^{eff}_{ij}\right)^4, \tag{3.13}$$

where

$$r^c_{ij} = \frac{\sigma^{nw}}{p^c_{ij}}, \tag{3.14}$$

$$r^{eff}_{ij} = \frac{1}{2} \left(\sqrt{\frac{r^2_{ij} - (4 - \pi) r^{c^2}_{ij}}{\pi}} + r_{ij} \right). \tag{3.15}$$

In (3.12), β is a resistance factor that depends on geometry, surface roughness, crevice roundness and other specifications of the cross-section. A detailed explanation of β can be found in Zhou, Blunt & Orr (1997). As mentioned earlier, the pore throat capillary pressure p^c_{ij} is set equal to the capillary pressure of the upstream pore body.

3.2.5. *Snap-off*

During drainage, if the local capillary pressure in a pore throat becomes smaller than a critical value of capillary pressure (defined below), the corner interfaces become unstable and snap-off will occur. Ignoring dynamics of contact angle, the criterion for snap-off in a square cross-section pore throat has been defined as follows (Vidales, Riccardo & Zgrabli 1998):

$$p^c_{ij} \leqslant \frac{\sigma^{nw}}{r_{ij}} (\cos\theta - \sin\theta). \tag{3.16}$$

After the snap-off, the pore throat will be filled with the wetting phase again, and the non-wetting phase becomes disconnected, receding in the neighbouring two pore bodies.

3.3. *Computational procedure*

3.3.1. *Pressure field solver*

Equations (2.4), (2.6) and (2.7) form a determinate set to be solved for s_i^w, p_i^w and p_i^n. However, to reduce the computational demand, the equations are reformulated in terms of total pressure (saturation-weighted average pressure, $\bar{p}_i$) defined in each pore body as

$$\bar{p}_i = s_i^w p_i^w + s_i^n p_i^n. \tag{3.17}$$

Using (2.4) and $s_i^n + s_i^w = 1$, we get the following equations for pressures of wetting and non-wetting phases:

$$p_i^w = \bar{p}_i - s_i^n p_i^c, \tag{3.18}$$

$$p_i^n = \bar{p}_i + s_i^w p_i^c. \tag{3.19}$$

For each pore body i, we know that the summation of fluxes of the two phases should be zero, as specified by (2.5). Substituting from (2.7) into (2.7), we obtain

$$\sum_{j=1}^{N_i} \left[K_{ij}^n \left(p_i^n - p_j^n \right) + K_{ij}^w \left(p_i^w - p_j^w \right) \right] = 0. \tag{3.20}$$

Substituting (3.18) and (3.19) in (3.20) results in an equation for $\bar{p}_i$:

$$\sum_{j=1}^{N_i} \left(K_{ij}^w + K_{ij}^n \right) (\bar{p}_i - \bar{p}_j) = -\sum_{j=1}^{N_i} \left[\left(K_{ij}^n s_i^w - K_{ij}^w \left(1 - s_i^w \right) \right) p_i^c + \left(K_{ij}^w \left(1 - s_j^w \right) - K_{ij}^n s_j^w \right) p_j^c \right]. \tag{3.21}$$

In this equation, the right-hand side as well as the coefficients of the left-hand side depend on local saturation only. This linear system of equations is solved for $\bar{p}_i$ by diagonally scaled bi-conjugate gradient method using the SLATEC mathematical library (Fong *et al.* 1993).

3.3.2. *Saturation update*

After calculating $\bar{p}_i$, pressure of phases can be back-calculated explicitly using (3.18) and (3.19). Then (2.7) can be used to calculate Q_{ij}^α. Afterwards, (2.6) can be solved for new saturations in an explicit way based on saturation values from the previous time step. This procedure, however, will result in numerical problems for a capillary-dominated flow regime, as mentioned in Thompson (2002). Thompson (2002) found that the explicit saturation update was not numerically stable for very small capillary numbers and he could not successfully simulate the capillary-dominated flow. In addition, he could not observe consistency between near-equilibrium snapshots resulting from dynamic simulations and quasi-static ones. Therefore, we have developed a semi-implicit approach to control the nonlinearities under such flow conditions. Summing (2.7) for the two phases and writing p_i^w in terms of p_i^n and p_i^c, we obtain the following relationship for the total flux $Q_{ij}^{tot} = Q_{ij}^n + Q_{ij}^w$ through a pore throat:

$$Q_{ij}^{tot} = \left(K_{ij}^n + K_{ij}^w \right) \left(p_i^n - p_j^n \right) - K_{ij}^w \left(p_i^c - p_j^c \right). \tag{3.22}$$

Then, defining $K_{ij}^{n} + K_{ij}^{w} = K_{ij}^{tot}$ and re-substituting for Q_{ij}^{n} from (2.7), we can write:

$$Q_{ij}^{tot} = \frac{K_{ij}^{tot}}{K_{ij}^{n}} Q_{ij}^{n} - K_{ij}^{w}\left(p_i^c - p_j^c\right). \tag{3.23}$$

Rewriting the above equation for Q_{ij}^{n}, we get a formula analogous to the fractional-flow equation:

$$Q_{ij}^{n} = \frac{K_{ij}^{n}}{K_{ij}^{tot}} Q_{ij}^{tot} + \frac{K_{ij}^{w} K_{ij}^{n}}{K_{ij}^{tot}}\left(p_i^c - p_j^c\right). \tag{3.24}$$

Substituting (3.24) in (2.6) results in

$$V_i \frac{\Delta s_i^w}{\Delta t} - \sum_{j=1}^{N_i}\left(\frac{K_{ij}^{n}}{K_{ij}^{tot}} Q_{ij}^{tot} + \frac{K_{ij}^{w} K_{ij}^{n}}{K_{ij}^{tot}}\left(p_i^c - p_j^c\right)\right) = 0. \tag{3.25}$$

The capillary pressure term can be approximated to the first order by

$$p_i^c - p_j^c = \frac{\partial p_{ij}^c}{\partial s_{ij}^w}\left(s_i^w - s_j^w\right), \tag{3.26}$$

where $\partial p_{ij}^c / \partial s_{ij}^w$ is calculated from the upstream pore body. Finally, after substitution of (3.26) in (3.25), we get the following discretized form of a semi-implicit equation for saturation update:

$$V_i \frac{\left(s_i^w\right)^{k+1} - \left(s_i^w\right)^{k}}{\Delta t} - \sum_{j=1}^{N_i}\left(\frac{K_{ij}^{n}}{K_{ij}^{tot}} Q_{ij}^{tot} + \frac{K_{ij}^{w} K_{ij}^{n}}{K_{ij}^{tot}} \frac{\partial p_{ij}^c}{\partial s_{ij}^w}\left(\left(s_i^w\right)^{k+1} - \left(s_j^w\right)^{k+1}\right)\right) = 0, \tag{3.27}$$

where the superscript k denotes time step level. In (3.27), all coefficients are evaluated at time step k, so that this equation may be recast into a linear equation matrix:

$$\left(\frac{V_i}{\Delta t} - \sum_{j=1}^{N_i} \frac{K_{ij}^{n} K_{ij}^{w}}{K_{ij}^{tot}} \frac{\partial p_{ij}^c}{\partial s_{ij}^w}\right)\left(s_i^w\right)^{k+1} + \left(\sum_{j=1}^{N_i} \frac{K_{ij}^{n} K_{ij}^{w}}{K_{ij}^{tot}} \frac{\partial p_{ij}^c}{\partial s_{ij}^w}\right)\left(s_j^w\right)^{k+1} = \frac{V_i}{\Delta t}\left(s_i^w\right)^{k} + \sum_{j=1}^{N_i} \frac{K_{ij}^{n}}{K_{ij}^{tot}} Q_{ij}^{tot}. \tag{3.28}$$

Note that since Q_{ij}^{tot} and K_{ij}^{α} are calculated from time step k, this scheme is not fully implicit. Here also the diagonally scaled bi-conjugate gradient method from SLATEC mathematical library (Fong *et al.* 1993) is used.

3.3.3. *Time stepping*

The time step is determined on the basis of time of filling of pore bodies by the non-wetting phase or wetting phase denoted by Δt_i. The wetting phase saturation of a pore body varies between 1 and $s_{i,min}^{w}$ as we assume that a pore body may be drained down to the minimum saturation. On the other hand, we allow for imbibition to occur locally in some pore bodies, in which case the wetting phase saturation in a pore body can go back to 1. Then, the global time step will be the minimum value of all local time steps. So, we calculate Δt_i for all pore bodies, depending on the process,

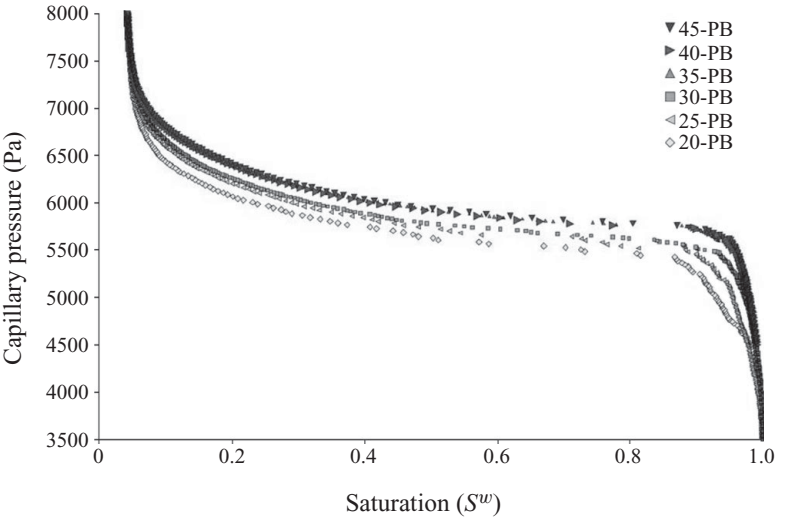

FIGURE 2. Quasi-static P^c–S^w curves for different network sizes.

from the following:

$$\Delta t_i = \begin{cases} \dfrac{V_i}{q_i^n}\left(s_i^w - s_{i,min}^w\right) & \text{for local drainage,} \quad q_i^n > 0, \\ \dfrac{V_i}{q_i^n}\left(1 - s_i^w\right) & \text{for local imbibition,} \quad q_i^n < 0, \end{cases} \tag{3.29}$$

where the accumulation rate of the non-wetting phase is defined as $q_i^n = \sum_{j=1}^{N_i} Q_{ij}^n$. Then, the time step is chosen to be the minimum Δt_i:

$$\Delta t_{global} = \min\{\Delta t_i\}. \tag{3.30}$$

Note that we have imposed a truncation criterion of 10^{-6} for saturation when it is close to $s_{i,min}^w$ or 1. Also, note that in (3.29), there is a correspondence between saturation change (numerator) and the accumulation rate of the non-wetting phase (denominator). That is, when local saturation is close to the limits, the accumulation rate of the non-wetting phase is also very small. This means that Δt_i always remains finite and non-zero.

4. Drainage simulations and analysis

4.1. *General procedure*

Initially, the network is fully saturated with the wetting phase. The simulation of drainage starts with raising the pressure of the non-wetting phase reservoir. When the global pressure difference, P_{global}^c, becomes larger than the entry pressure of the largest pore throat connected to the non-wetting phase reservoir, drainage starts. In quasi-static simulations, the global pressure difference is increased incrementally. At the end of each step, when there is no flow (static conditions), the overall saturation of the network is determined. Then, the global pressure difference is increased again.

In order to have representative results for a network with a given statistical distribution, the network must have a minimum size, corresponding to the REV (Bear 1972). REV size was determined by performing quasi-static drainage simulations for a network with different sizes but with the same statistical parameters. Results are shown in figure 2. It is evident that the P^c–S^w curve changes with the network size

until a network size of $35 \times 35 \times 35$ pore bodies. For larger network sizes, the curves are almost identical. Therefore, a network with 35 pore bodies in each direction was used in our simulations.

4.2. *Averaging procedure*

Our simulations result in local-scale variables such as pressure, saturation and fluxes. These have to be averaged over the network to obtain macroscopic variables. Average saturation is simply defined as follows:

$$\left.\begin{aligned} S^w = \frac{V^w}{V^w+V^n} = \frac{\sum_{i=1}^{n_{pb}} s_i^w V_i}{\sum_{i=1}^{n_{pb}} V_i}, \\ S^n = 1 - S^w, \end{aligned}\right\} \tag{4.1}$$

where n_{pb} is the total number of pore bodies. The total flux across any given surface is equal to the sum of fluxes of all pore throats intersecting that surface. The averaging of pressure is, however, less straightforward. Commonly, average pressure is obtained using an intrinsic phase average operator (see e.g. Whitaker 1977). However, recently it has been shown that the intrinsic phase average pressure introduces numerical artefacts when both pressure and saturation are spatially variable (see Nordbotten *et al.* 2007, 2008). Instead, a centroid-corrected averaging operator has been suggested by Nordbotten *et al.* (2008) to alleviate problems associated with intrinsic phase averaging. Nevertheless, here we still use intrinsic phase average for a pore body i with volume of V_i and α-phase pressure of p_i^α, as this is still most commonly used:

$$P^\alpha = \frac{1}{\delta V^\alpha}\int_{\delta V^\alpha} P^\alpha \mathrm{d}V = \frac{\sum_{i=1}^{n_{pb}} p_i^\alpha s_i^\alpha V_i}{\sum_{i=1}^{n_{pb}} s_i^\alpha V_i}, \quad \alpha = n, w. \tag{4.2}$$

Commonly, the macroscale capillary pressure is defined to be the difference in the average pressures of non-wetting and wetting phases. But as we show later, this is not a correct definition of macroscopic capillary pressure. Here, we propose to define macroscopic capillary pressure based on the average of local capillary pressures of pore bodies, weighted by the corresponding interfacial area A_i^{nw}:

$$P^c = \frac{\sum_{i=1}^{n_{pb}} p_i^c A_i^{nw}}{\sum_{i=1}^{n_{pb}} A_i^{nw}}. \tag{4.3}$$

The calculation of interfacial area in pore bodies is explained in Appendix B.

5. Results and discussion

5.1. *Quasi-static versus dynamic simulation*

As explained before, previous dynamic pore-network models failed to simulate very slow flow (very small capillary numbers) properly. As Thompson (2002) and Al-Gharbi & Blunt (2005) found that the application of dynamic pore-network models

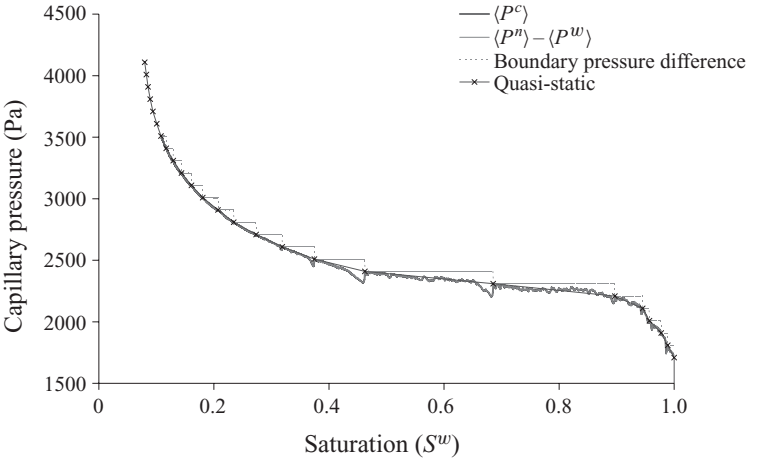

FIGURE 3. Comparison between equilibrium points resulting from quasi-static and dynamic pore-network models for the same boundary conditions in a 20-pore body cubic lattice network.

for very small capillary numbers (relatively low flow velocities) was not numerically successful and severe instability problems were observed. To show capability of the proposed algorithm in simulating a capillary-dominated flow, the P^c–S^w curve has been produced using the dynamic pore-network model with very small non-wetting phase reservoir pressure increments. Simultaneously, for the same network the P^c–S^w curve has been generated using a quasi-static pore-network model. As can be observed in figure 3, the equilibrium points resulting from both models are the same. That is, if there is no dynamic effect in contact angle, there will be full agreement between quasi-static and dynamic pore-network models. We found that equilibrium fluid configurations resulting from both models (not shown here) are the same. This simulation was done for a 20-pore body cubic lattice network. The simulation took 46 h on Intel(R) CPU 6600, 2.4 GHz with 2 GB RAM, which is significantly more time-consuming compared with viscous-dominated flow.

Figure 3 shows some interesting features resulting from the behaviour of interfaces in a near-to-equilibrium system. Average phase pressure difference, $P^n - P^w$ (4.2), and average capillary pressures P^c (4.3) are the same, and their values are fluctuating around the quasi-static model P^c–S^w curve. The dips visible in figure 3 are due to the relaxation of the interfaces behind the invading fronts. This phenomenon has been observed in micromodel experiments reported by Pyrak-Nolte (2007). However, as we increased the aspect ratio (radius of pore body to radius of pore throat), these dips disappeared, but more fluctuations in the dynamic P^c–S^w curve were observed.

5.2. *Non-equilibrium effects in average phase pressures*

In this section, we investigate the validity of non-equilibrium capillarity in (1.7) and the behaviour of non-equilibrium capillarity coefficient (τ). To do so, we have determined the change of saturation with time under various dynamic conditions and have prepared corresponding plots of average phase pressure difference versus saturation.

As explained before, by imposing a large global pressure difference on the network domain, it is possible to simulate dynamic two-phase flow drainage experiments. We have considered two fluids with three different viscosity ratios ($M = \mu^n/\mu^w = 0.1, 1, 10$)

and five different global pressure difference values (10, 15, 20, 25 and 30 kPa). Computational time increases with the decrease of viscosity ratio and decrease of global pressure difference. The simulations took about 10–70 h on Intel(R) CPU 6600, 2.4 GHz with 2 GB RAM.

Commonly, for viscosity ratios less than unity, the displacement shows instability. We found that for given flow conditions, saturation changes with time for $M = 1$ and $M = 10$ were very similar. The breakthrough saturations for $M = 1$ and $M = 10$ were not so different for different global pressure differences. While for $M = 0.1$, the breakthrough saturation decreased significantly for larger global pressure differences. The breakthrough saturation for favourable viscosity ratio was smaller than that for the unfavourable viscosity ratio (in the same network), due to the stable front invasion for $M \geqslant 1$ and viscous fingering for $M < 1$.

Curves of average fluid pressure difference (based on definition (4.2)) versus average saturation are shown in figure 4. It is clear that the curves are strongly dependent on boundary conditions. The differences in fluid pressures are found to be higher for larger global pressure differences, which also lead to larger saturation changes. This behaviour agrees with (1.7), which suggests larger pressure differences for large saturation changes under drainage.

As can be observed in figure 4, a higher-viscosity ratio can also cause higher pressure build-up. Higher-viscosity ratios mean that less snap-off occurs and fewer pores will be partially filled and disconnected from the reservoir. The decline in the fluid pressure differences as residual saturation is approached is due to the non-wetting phase breaking through the outflow boundary of the averaging window. After the breakthrough, average phase pressure difference decreases because of the direct connection of non-wetting phase to the lower (outflow) boundary, which entraps wetting phase in the corners. Thus, wetting fluid will gain a higher pressure compared with non-trapped wetting phase. Consequently, the average pressure difference approaches the P^c–S^w curve. The decline in the fluid pressure differences as residual saturation in the averaging window is reached has been studied analytically by Nordbotten *et al.* (2008), who found qualitatively the same behaviour.

According to (1.7), the deviation of the macroscopic pressure difference from the macroscopic capillary pressure is related to the time rate of change of saturation. Hassanizadeh & Gray (1993*a*) have suggested that τ is a non-negative non-equilibrium capillarity coefficient that may still depend on saturation. To implement this equation for practical purposes, it is crucial to determine the dependency of this coefficient on medium and/or fluid properties. To compute τ, first a set of $\partial S^w/\partial t$ values is calculated for a given saturation (and constant M). Then, from corresponding curves in figure 4, P^c and $P^n - P^w$ are found at that saturation (for a given viscosity ratio M). This results in a graph of $P^n - P^w - P^c$ versus $\partial S^w/\partial t$ (not shown here) for the given saturation values and viscosity ratios. The slopes of the resulting curves give the values of τ at different saturations. Results are plotted in figure 5. It is evident that the dynamic effect is stronger for higher-viscosity ratios. This is because for viscous fluids, it takes much longer time for the equilibrium fluid configuration to be reached. The decrease of τ after the breakthrough is not relevant and is not a property of the porous medium, but is due to the drainage front reaching the boundary of the domain (see also the explanation given in relation to the decline of pressure differences at low saturation in figure 4). For $M \geqslant 1$, the non-equilibrium capillarity coefficient increases with the decrease of the wetting phase saturation, which is similar to the findings of Mirzaei & Das (2007) in their column-scale drainage simulations (using a continuum model) for a favourable viscosity ratio. But this trend is reversed for $M = 0.1$. This

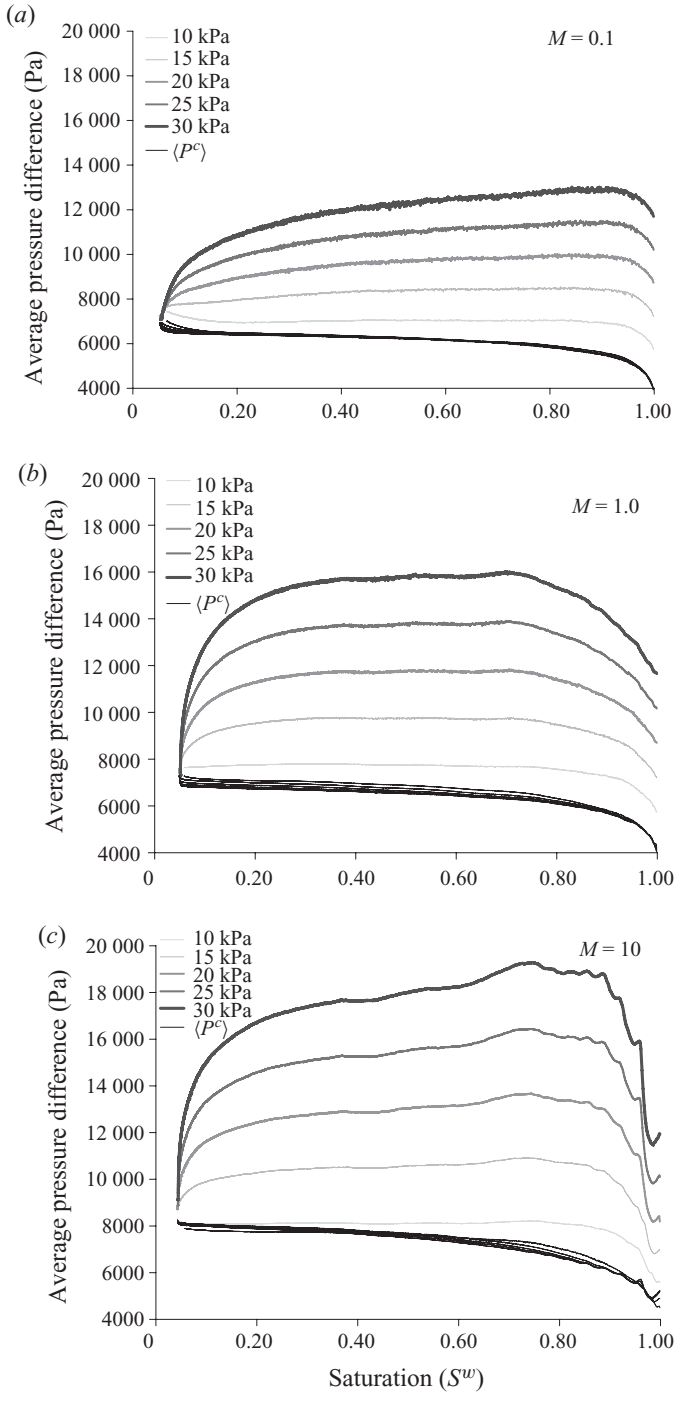

FIGURE 4. Average phase pressure difference curves P^n–P^w calculated using (4.2) and average capillary pressure curves P^c calculated using (4.3) for five different global pressure differences and viscosity ratios (*a*) $M = 0.1$, (*b*) $M = 1$ and (*c*) $M = 10$.

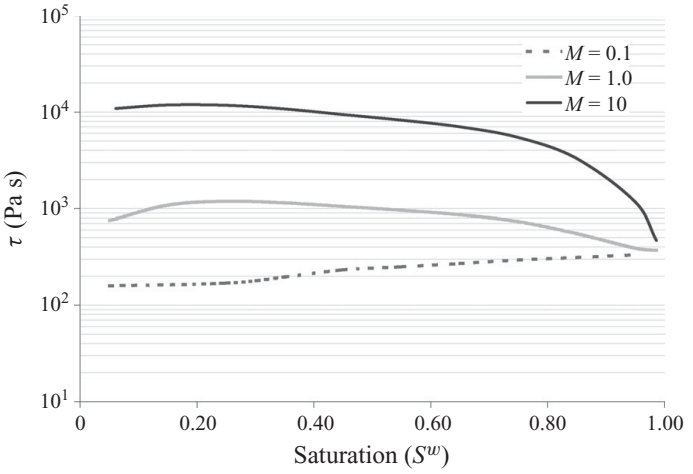

FIGURE 5. Variation of non-equilibrium capillarity coefficient τ as a function of saturation for different viscosity ratios $M = 0.1, 1.0, 10$. The vertical axis is shown in logarithmic scale.

trend can be interpreted based on the empirical equation suggested by Stauffer (1978) for unsaturated soil. On the basis of the drainage experiments done on fine sand in an air–water system, he suggested the following equation:

$$\tau = \frac{\alpha \epsilon \mu}{\lambda k} \left(\frac{p^c}{\rho g} \right)^2, \tag{5.1}$$

where α is assumed to be a constant equal to 0.1 for granular soils, ϵ is porosity, μ is the water viscosity, λ and p^c are the coefficients in Brooks–Corey formula (Brooks & Corey 1964), k is the saturated permeability, ρ is the water mass density, and g is the gravity. For the case of two-phase flow, μ can be replaced by μ_{eff}, the saturation-weighted average viscosity of the two fluids, which is very much dependent on the flow regime. For a stable invasion, where a piston-like movement is dominant, viscosity can be weighted linearly with saturation: $\mu_{eff} = \mu^n S^n + \mu^w S^w$. However, for a viscous fingering regime, some researchers such as Koval (1963) have suggested some other empirical relationships for effective viscosity (see e.g. Fayers, Blunt & Christie 1990). In all equations, effective viscosity is suggested to be a function of saturation. Considering $\tau \propto \mu_{eff}$, it can be concluded that $\partial\tau/\partial S^w \propto \partial\mu_{eff}/\partial S^w$. The term $\partial\mu_{eff}/\partial S^w$ will be positive for unfavourable viscosity ratio, since both wetting phase saturation and effective viscosity decrease with decreasing of wetting phase saturation. In addition, the difference between magnitudes of $\partial\tau/\partial S^w$ for different viscosity ratios is significant. From figure 5, we can determine that $\partial\tau/\partial S^w$ for $M = 10$ is almost 10 times larger than that for $M = 1$. This is qualitatively consistent with (5.1), where effective viscosity for $M = 10$ is almost 10 times larger than that for $M = 1$ for intermediate and low ranges of wetting phase saturation.

5.3. *On the existence of the P^c–S^w–a^{nw} surface*

As discussed in § 1, the main underlying concept in (1.7) is that capillary pressure is an intrinsic property of the fluids–solid system, and thus it should be a function of state variables only (namely saturation, temperature and specific interfacial area); it should not depend on initial or boundary conditions and other parameters that

control transient flow conditions such as viscosity. Here, we investigate this conjecture for the case of primary drainage.

First, consider the average capillary pressure P^c defined by (4.3). Plots of P^c versus average saturation under various dynamic conditions are shown in figure 6(*a*), where the quasi-static capillary pressure is also plotted. It is evident that the average capillary pressure–saturation relationship is not unique, as it depends on transient flow conditions as well as fluids viscosity ratio. This apparently contradicts the concepts presented above, which state that capillary pressure curve is an intrinsic property of the fluid–solid system. But in fact the theory prescribes that the capillary pressure is a function of specific interfacial area as well as saturation (see e.g. Hassanizadeh & Gray 1993*a*; Reeves & Celia 1996; Held & Celia 2001; Joekar-Niasar *et al.* 2008, 2009). So, differences observed in P^c–S^w curves could be due to the fact that the specific interfacial area is different under different dynamic conditions.

Figure 6(*b*) shows values of specific interfacial area for different viscosity ratios at different saturations for a three-dimensional network used in previous simulations. In addition, the relationship between specific interfacial area and saturation resulting from static simulations is shown by a thick solid line. According to the conjecture of Hassanizadeh & Gray (1993*b*), if the P^c–S^w–a^{nw} surface were an intrinsic property of the porous medium, all the points for all non-equilibrium and equilibrium conditions should be located on a single surface. To investigate this, a second-order polynomial surface was fitted to all P^c–S^w–a^{nw} data points presented in figures 6(*a*) and 6(*b*), which is shown in figure 6(*c*). Note that the selection of a polynomial function for fitting is arbitrary and only for simplicity in presentation. This surface is highly correlated with the data points ($R^2 = 0.95$ and the average relative error is about 14 %). The behaviour of the surface is very similar to the P^c–S^w–a^{nw} surfaces shown by Reeves & Celia (1996), Held & Celia (2001), Joekar-Niasar *et al.* (2008, 2009) and Porter *et al.* (2009), although they only simulated P^c–S^w–a^{nw} equilibrium points.

As can be observed, specific interfacial area has larger values for smaller viscosity ratios, as a result of instability and fingering. For an unfavourable viscosity ratio ($M = 0.1$), local entry capillary pressures of pore throats and their connectivity (topology and geometry) control the invasion. According to results shown in figure 6(*b*), the largest specific interfacial area has been created in the quasi-static simulation, where only capillary forces are controlling the invasion. In other words, it seems that for a given saturation value, with the decrease of viscous forces compared with capillary forces, more interfacial area is created.

A significant variation of specific interfacial area with viscosity ratio and flow conditions in figure 6(*b*) suggests that invasion mechanism and system parameters have a major effect on interfacial area evolution under dynamic conditions. This is illustrated in figure 7, where we have shown different snapshots of fluid distribution for drainage. These simulations were performed in a two-dimensional network with size of 70×70 pore bodies. Snapshots are shown for $P^c_{global} = 20$ kPa and at wetting phase saturations of 0.9, 0.5 and 0.3. As shown in figure 7, under favourable conditions ($M \geqslant 1$), the interface front is stable with less fingering. For a small global pressure difference, more fingering occurs compared with high global pressure differences for a given (favourable) viscosity ratio. This is because, with more invasion of the non-wetting fluid, more energy dissipation occurs, and consequently at low saturations more fingering can occur. Under unfavourable conditions ($M < 1$), however, even a large global pressure difference cannot stabilize the interface front. This is because the front basically follows the local variations in pore throat sizes within the pore network (Aker *et al.* 1998*b*).

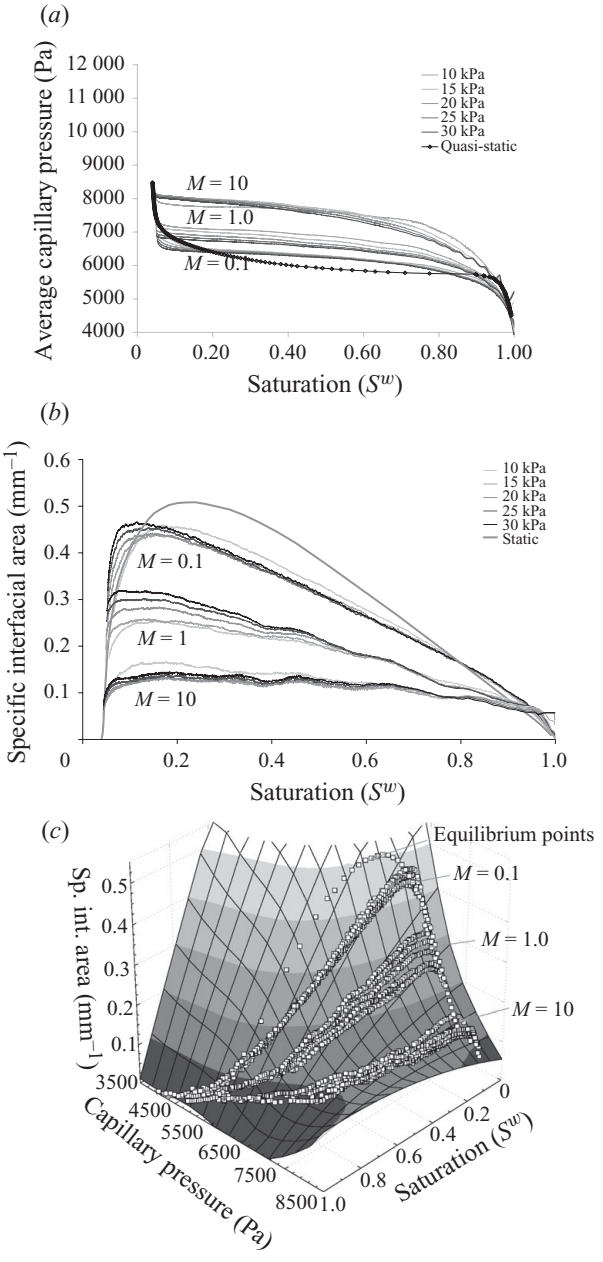

FIGURE 6. (*a*) Macroscopic capillary pressure defined by (4.3) for five different global pressure differences and three different viscosity ratios $M = 0.1, 1.0, 10$ compared with quasi-static capillary pressure curve in a three-dimensional ($35 \times 35 \times 35$) network. (*b*) A quantitative comparison between quasi-static and dynamic specific interfacial area–saturation curves for the same fluid–solid properties and boundary conditions mentioned in (*a*). (*c*) A second-order polynomial surface fitted to all P^c–S^w–a^{nw} data points resulting from dynamic and quasi-static simulations shown in (*a*) and (*b*) ($R^2 = 0.95$).

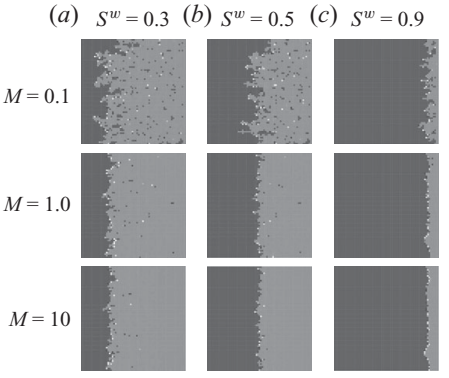

FIGURE 7. Qualitative comparison of macroscopic interface topology for $M = 0.1$, 1.0 and 10 in a two-dimensional (70×70) network at three different saturations.

5.4. *Production rate of specific interfacial area versus saturation*

As explained in § 1, in the new theory of two-phase flow, the interfacial area production term E^{nw} (1.4) plays a significant role. Since there is as yet no quantitative information available about this term, we have used our pore-network model to get some insight into its dependence on other primary variables. In particular, the dependency of E^{nw} on saturation and its time rate of change, and on viscosity ratio will be studied.

The procedure for the estimation of E^{nw} is as follows. If in (1.4) we neglect the advective flux term, the production term may be calculated as the rate of change of specific interfacial area with time. The production rate of specific interfacial area (E^{nw}) is plotted as a function of saturation in figure 8. It is evident that E^{nw} decreases with the decreasing of saturation. We also see that it is much larger for $M = 0.1$ than that for $M = 10$ and $M = 1$. Figure 8 also shows that E^{nw} depends on the imposed boundary pressure, which in turn causes different rate of change of saturation $\partial S^w/\partial t$. Therefore, on the basis of figure 8 and the change of saturation with time, one can construct a relationship between E^{nw} and $-\partial S^w/\partial t$ for different saturations. The results (not presented here) show that at saturations lower than 0.9, we can roughly define a linear relationship between E^{nw} and $-\partial S^w/\partial t$:

$$E^{nw} = -G\frac{\partial S^w}{\partial t}, \tag{5.2}$$

where $G\left[L^{-1}\right]$ is a material coefficient, which itself is a function of saturation as well as viscosity ratio, as shown in figure 9. We suggest a linear relationship between G and saturation: $G(S^w, M) = a + b\,S^w$, where values of 'a' and 'b' depend on viscosity ratio and are reported in figure 9. A relationship similar to (5.2) was employed by Niessner & Hassanizadeh (2008) in a model based on the new theory of two-phase flow.

6. Summary and conclusions

The DYPOSIT model, a dynamic pore-network model for simulating two-phase flow in a porous medium has been developed. The combination of features included in this model has not been offered in previous network models. The network elements have square cross-sections, as a result of which both phases can be simultaneously presented within a pore body or pore throat. Local capillary pressure in the pore elements is taken into account. Two different pressure fields are assigned to each phase and solved

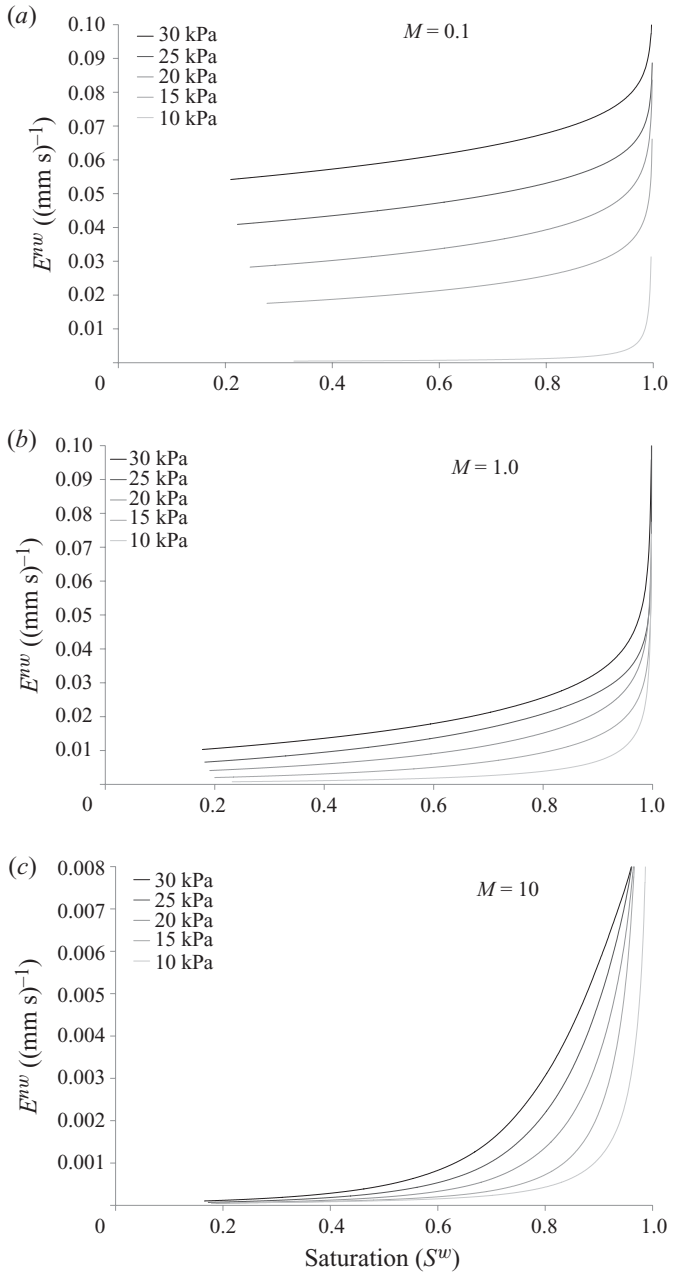

FIGURE 8. Plots of production rate of specific interfacial area E^{nw} versus saturation for (*a*) $M = 0.1$, (*b*) $M = 1.0$ and (*c*) $M = 10$, and for various values of global pressure difference.

using a robust algorithm. The model is numerically stable for a wide range of viscosity ratios and under different dynamic conditions (viscous-dominated or capillary-dominated). The model is used to simulate drainage experiments with Dirichlet boundary conditions. It is applied to the study of dynamics of specific interfacial area, average capillary pressure, average phase pressure differences, functionality of non-equilibrium capillarity coefficient as well as production rate of interfacial area.

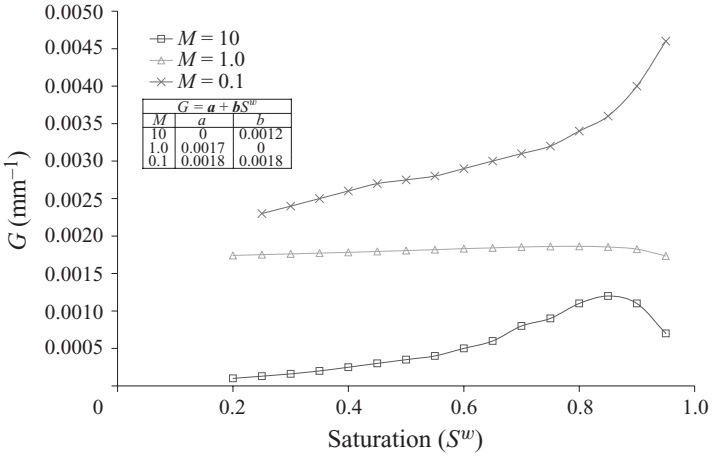

FIGURE 9. Relationship between G and the wetting phase saturation for different viscosity ratios.

Macroscopic capillary pressure is defined as the average of local capillary pressure at all interfaces weighted with the area of the interface. We have shown that neither average capillary pressure–saturation curves nor specific interfacial area–saturation curves are unique, but they depend on flow dynamics as well as fluid–solid properties. However, it is shown that capillary pressure–saturation–interfacial area surface for primary drainage is an intrinsic property of the porous medium, independent of fluid properties and dynamic conditions. The difference between average phase pressures, however, is found to be dependent on boundary pressures and time rate of change of saturation as prescribed by the dynamic capillary theory. Our results illustrate that the non-equilibrium capillarity coefficient is a function of saturation as well as viscosity ratio.

Dynamics of interfacial area show that with the decrease of the viscosity ratio, specific interfacial area increases, which is a consequence of the invasion mechanism. However, in all dynamic cases, specific interfacial area is smaller than that under quasi-static conditions. With the decrease of the viscosity ratio, the effect of the intrinsic properties of medium (geometry and topology) on the creation of interfacial area increases. The production rate of specific interfacial area for different viscosity ratios has been studied and quantified. With the decrease of the viscosity ratio, the production rate of the specific interfacial area increases. The production rate is found to have an almost linear relationship with the time rate of change of saturation. This linearity coefficient is a function of saturation as well as the viscosity ratio. The dynamic pore-network model developed here is capable of simulating complex problems of flow of two fluid phases in porous media including non-equilibrium capillarity effects and dynamics of interfaces. In future research, our model will be applied to a larger domain in order to simulate column experiments and investigate the validity of the full system of equations of the extended Darcy's law (1.1) and (1.2).

We are grateful to Professor A. Leijnse and Professor R. Helmig for valuable comments and fruitful discussions. The authors are members of the International Research Training Group NUPUS, financed by the German Research Foundation (DFG) and The Netherlands Organization for Scientific Research (NWO). This research was supported by Utrecht Centre for Geosciences and in part by the

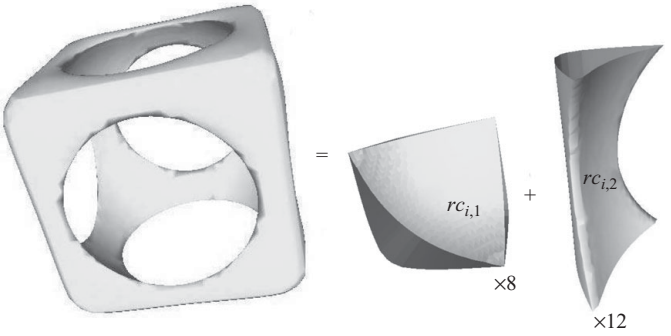

FIGURE 10. A pore body occupied by the non-wetting phase (middle) and the wetting phase in corners and edges. There are wetting–non-wetting interfaces in 8 corners with mean radius of $rc_{i,1}$ and in 12 edges with mean radius of $rc_{i,2}$.

Norwegian Research Council, StatoilHydro, and Norske Shell under grant 178013/13. We acknowledge anonymous reviewers for their very useful comments.

Appendix A. The p_i^c–s_i^w relationship for a pore body

Consider a cube with its inscribed sphere radius equal to R_i; so the edge length is equal to $2R_i$. If the non-wetting phase volume is larger than the volume of the inscribed sphere (i.e. $s^w_{insc.} \leqslant 1-(\pi/6)=0.48$), the fluid interfaces are pinned into the corners. However, for $s^w_{insc.} > 1-(\pi/6)=0.48$, they are not pinned into the corners. Therefore, for the variation of local capillary pressure with saturation, we identify two different zones, as shown in figure 12 and described below.

A.1. *Capillary pressure for* $0 < s_i^w \leqslant 0.48$ *(zone I)*

In a cube, interfaces can be formed along its 12 edges as well as in its 8 corners, as shown in figure 10. Edge interfaces form part of a cylindrical surface. Therefore, they have only one finite radius of curvature. Corner interfaces form part of a spherical surface and thus have two identical finite curvatures. Assuming a contact angle of zero, edge interfaces form one-fourth of a cylinder, whereas corner interfaces are one-eighth of a sphere (see figure 10). Let us denote the radius of curvature of corner interfaces by $rc_{i,1}$. Then, the total volume of the wetting phase in the corners would be equal to the volume of a cube with dimensions $2rc_{i,1}$ minus the volume of a sphere with radius $rc_{i,1}$:

$$V^w_{corner} = \left(8 - \frac{4}{3}\pi\right) rc^3_{i,1}. \tag{A 1}$$

The length of an edge interface is equal to the cube size, $2R_i$, minus two times the radius of corner interfaces:

$$L_{edge} = 2(R_i - rc_{i,1}). \tag{A 2}$$

Thus, if we denote the radius of curvature of an edge interface by $rc_{i,2}$, the total volume of the wetting phase in the edges will be

$$V^w_{edge} = 12 L_{edge} rc^2_{i,2}\left(1 - \frac{\pi}{4}\right). \tag{A 3}$$

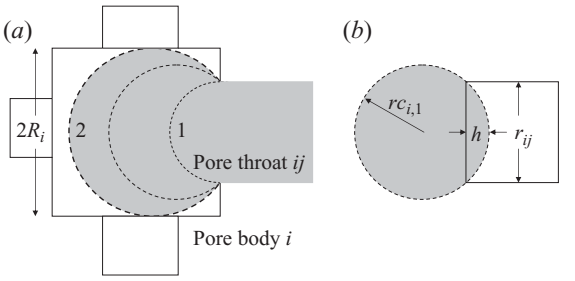

FIGURE 11. (*a*) Expansion of an interface into a pore body before inscribing in it. (*b*) Parametrization of the interface for calculating the volume of non-wetting phase; h is the height of dome inside a pore throat (truncated part of the sphere), rc_1 is the radius of the expanding non-wetting sphere, and r_{ij} is the pore throat radius.

The total volume of the wetting phase in the pore body is thus obtained by summing (A 1) and (A 3) as

$$V_i^w = \left(8 - \frac{4}{3}\pi\right) rc_{i,1}^3 + 24(R_i - rc_{i,1}) rc_{i,2}^2 \left(1 - \frac{\pi}{4}\right). \tag{A 4}$$

Since we assume that the capillary pressure in a pore body is the same everywhere, the capillary pressures of edge and corner interfaces must be equal. Thus, $p_i^c = (2\sigma^{nw}/rc_{i,1}) = (\sigma^{nw}/rc_{i,2})$, which gives $rc_{i,1}$ and $rc_{i,2}$ in terms of p_i^c. Substituting for $rc_{i,1}$ and $rc_{i,2}$ in (A 4) and dividing both sides by the total volume of the cubic pore body, $8R_i^3$, we obtain the following p_i^c–s_i^w relationship for a pore body if $s_i^w \leqslant 0.48$:

$$s_i^w = \frac{\left(2 + \frac{1}{6}\pi\right)\left(\frac{2\sigma^{nw}}{p_i^c}\right)^3 + \left(6 - \frac{3}{2}\pi\right) R_i \left(\frac{2\sigma^{nw}}{p_i^c}\right)^2}{8R_i^3}. \tag{A 5}$$

The case of $rc_{i,1} = R_i$ corresponds to the situation that the non-wetting phase occupies the inscribed circle of the pore body.

A.2. *Capillary pressure for* $0.48 < s_i^w \leqslant 1$ *(zone II)*

When the fluid interfaces are not pinned into the corners, one may choose from the following two approaches.

(*a*) The simplest approach is to assign a constant capillary pressure equal to $2\sigma^{nw}/R_i$ to the pore body if $s_i^w \geqslant 0.48$ as shown in figure 12 (the horizontal line in zone II).

(*b*) The second approach is to assume that a capillary pressure varies with saturation. At the moment of invasion of the non-wetting fluid into a pore body, the local capillary pressure is close to the (entry) capillary pressure of the pore throat from which the fluid enters the pore body (figure 11). So, it is larger than the entry capillary pressure of the pore body, which is associated with that of the inscribed circle. As the interface moves into the pore body, it expands and its capillary pressure decreases. We assume that the interface goes through the following stages.

(i) First, as it enters the pore body, its radius remains unchanged, equal to the radius of the pore throat, r_{ij} (interface 1 in figure 11*a*). So, for the range $s_i^w \geqslant 1 - (2\pi/3)((r_{ij}/2R_i)^3)$, the local capillary pressure will be equal to the entry capillary pressure of the pore throat; $p_i^c = p_{e,ij}^c$.

(ii) From this point on, the radius of interface increases. For a given radius of curvature $rc_{i,1}$, the non-wetting fluid will be present within a truncated sphere as shown in figure 11(*b*). Defining $\widetilde{rc}_{i,1} = rc_{i,1}/2R_i$ and $\widetilde{r}_{ij} = r_{ij}/2R_i$, s_i^w can be calculated

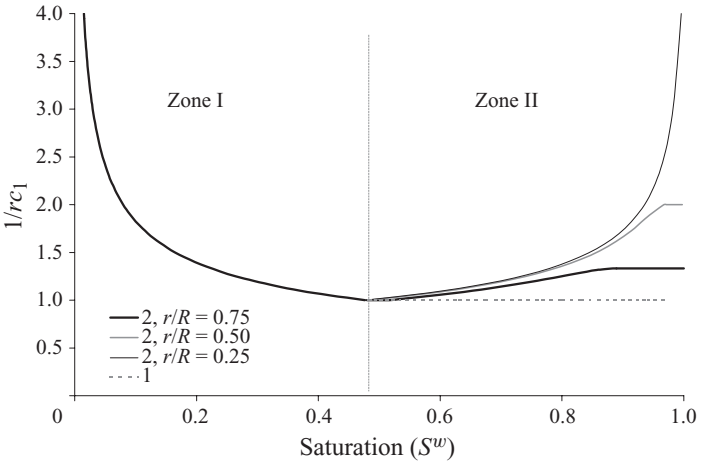

FIGURE 12. Local p_i^c–s_i^w curve during drainage for approach 1 (broken curve) and approach 2 (continuous curves). For approach 2, three different curves for three different aspect ratios have been shown.

as follows:

$$s_i^w = 1 - \frac{\pi}{8}\left(\frac{2}{3}\widetilde{rc}_{i,1}^3 - \widetilde{rc}_{i,1}^2\sqrt{\widetilde{rc}_{i,1}^2 - \widetilde{r}_{ij}^2} + \frac{1}{3}\left(\widetilde{rc}_{i,1}^2 - \widetilde{r}_{ij}^2\right)^{3/2}\right) \tag{A 6}$$

and $p_i^c = 2\sigma^{nw}/rc_{i,1}$.

(iii) At some point, the interface touches the sides of the pore body cube. Its radius of curvature is then equal to R_i (interface 2 in figure 11*a*) and the wetting phase saturation at this point is obtained from (A 6) by setting $rc_{i,1} = 1$; it is $s_i^w = 1 - (\pi/12) + (\pi/8)\sqrt{1 - \widetilde{r}_{ij}^2} - (\pi/24)(1 - \widetilde{r}_{ij}^2)^{3/2}$. From this point on, the non-wetting phase is in contact with the sidewalls of the pore body (relative to the pore throat) and it continues moving into the pore body, at the constant radius, until it is fully inscribed within the pore body. So, the wetting phase saturation reduces to 0.48. In this range, the local capillary pressure remains constant equal to $p_i^c = 2\sigma^{nw}/R_i$.

A plot of the local capillary pressure as a function of saturation for these two approaches has been shown in figure 12. As can be observed, depending on the size of the pore throat, the second approach can result in different p_i^c–s_i^w curves. With the increase of ratio of pore throat to pore body radii, the curves from the two approaches get closer to each other.

A.3. *Local p_i^c–s_i^w relationship for the full range of saturation*

Finally, to investigate the effect of these two assumptions on average behaviour of the model during drainage, a number of simulations were performed, with viscosity ratio set equal to 0.1 and the global pressure difference (P_{global}^c) set to 10 kPa. Change of saturation with time and change of average capillary pressure with saturation are shown in figure 13. As can be observed, the choice of local capillary pressure curve for the range $0.48 \leqslant s_i^w \leqslant 1$ is really small. This is due to the fact that only a few pores are partially filled in this range. As the simulation with the second approach is more time-consuming (it requires smaller time steps), we have used the curve from the first approach in all simulations in this paper.

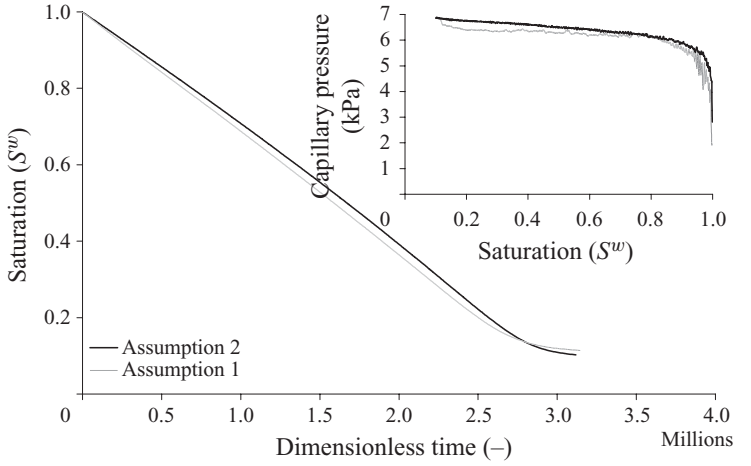

FIGURE 13. Effect of local p_i^c–s_i^w curve on the variation of saturation and capillary pressure versus time ($M = 0.1$, $P^c_{global} = 10$ kPa, $\overline{r/R} = 0.45$).

The resulting p_i^c–s_i^w curve for the full range of saturation was fitted by the following continuous function:

$$p_i^c = \frac{2\sigma^{nw}}{R_i\left(1 - \exp\left(-6.83 s_i^w\right)\right)}. \tag{A 7}$$

The radius of the curvature of corner interfaces is then approximated by the following formula:

$$rc_{i,1} = \frac{2\sigma^{nw}}{p_i^c} = R_i\left(1 - \exp\left(-6.83 s_i^w\right)\right). \tag{A 8}$$

Appendix B. The A_i^{nw}–s_i^w relationship for a pore body

As mentioned earlier, the volume of pore throats is assumed to be negligible compared with the volume of pore bodies. Thus, we neglected saturation of fluids in the pore throats. Similarly, we have not considered in our calculations the interfacial area present in pore throat corners.

There are two different types of capillary interfaces in a pore body: interfaces in corners and edges, and interfaces covering the entrance of pore throats that have not yet been invaded. These two types are referred to as 'corner interfaces' (arc menisci) and 'main terminal menisci', respectively (Mason & Morrow 1987).

B.1. *Corner interfaces*

Given a pore body with inscribed radius R_i filled with non-wetting and wetting phases, the non-wetting phase volume can be smaller or larger than the inscribed sphere volume. If the non-wetting phase volume is smaller than or equal to the volume of inscribed sphere, we assume that it occupies a sphere, whose radius is $R_{i,eq} = R_i((6/\pi)(1 - s_i^w))^{1/3}$. The corresponding interfacial area will be $4\pi R_{i,eq}^2$. If the non-wetting phase volume is larger than or equal to the volume of inscribed sphere, the wetting phase occupies geometries that were described in Appendix A. The interfaces will have the mean radius given by (A 8). Therefore, the total interfacial area in corners of a pore body will be equal to $4\pi R_{i,eq}^2 + 6\pi R_{i,eq}(R_i - R_{i,eq})$ for non-wetting phase saturations larger than the inscribed sphere. The results are summarized as

follows:

$$R_{i,eq} = \begin{cases} R_i\left((6/\pi)\left(1 - s_i^w\right)\right)^{1/3}, & s_i^w \geqslant 0.48, \\ R_i\left(1 - \exp\left(-6.83 s_i^w\right)\right), & s_i^w < 0.48, \end{cases} \tag{B 1}$$

$$A_i^{nw} = \begin{cases} 4\pi R_{i,eq}^2, & s_i^w \geqslant 0.48, \\ 4\pi R_{i,eq}^2 + 6\pi R_{i,eq}(R_i - R_{i,eq}), & s_i^w < 0.48. \end{cases} \tag{B 2}$$

B.2. *Main terminal menisci*

Consider a pore body i, partially occupied by the non-wetting phase, and a pore throat ij, which has not yet been invaded. The opening of the pore throat ij is thus covered by a meniscus, to which we refer as 'main terminal meniscus'. The geometry of the main terminal meniscus is simply assumed to be a part of a sphere with a radius of curvature R_{dm} equal to $2\sigma^{nw}/p_i^c$ similar to the interface within the pore throat in figure 11(b). Thus, the area of the main terminal meniscus will be equal to $8\pi\left(\sigma^{nw}/p_i^c\right)^2\left(1 - \sqrt{1 - (r_{ij}\, p_i^c/2\sigma^{nw})^2}\right)$.

REFERENCES

Aker, E. K., Maloy, J., Hansen, A. & Batrouni, G. G. 1998*a* A two-dimensional network simulator for two-phase flow in porous media. *Transport Porous Media* **32**, 163–186.

Aker, E. K., Maloy, K. J. & Hansen, A. 1998*b* Simulating temporal evolution of pressure in two-phase flow in porous media. *Phys. Rev.* E **58**, 2217–2226.

Al-Gharbi, M. S. & Blunt, M. J. 2005 Dynamic network modelling of two-phase drainage in porous media. *Phys. Rev.* E **71**, 016308.

Avraam, D. G. & Payatakes, A. C. 1995*a* Generalized relative permeability coefficients during steady-state, two-phase flow in porous media and correlation with the flow mechanisms. *Transport Porous Media* **20**, 135–168.

Azzam, M. I. S. & Dullien, F. A. L. 1977 Flow in tubes with periodic step changes in diameter: a numerical solution. *Chem. Engng Sci.* **32**, 1445–1455.

Bear, J. 1972 *Dynamics of Fluids in Porous Media*. Elsevier.

Blunt, M., Jackson, M. D., Piri, M. & Valvatne, P. H. 2002 Detailed physics, predictive capabilities and macroscopic consequences for pore-network models of multiphase flow. *Adv. Water Resour.* **25**, 1069–1089.

Blunt, M. & King, P. 1990 Macroscopic parameters from simulations of the pore scale flow. *Phys. Rev.* A **42**, 4780–4788.

Blunt, M. & King, P. 1991 Relative permeabilities from two- and three-dimensional pore-scale network modelling. *Transport Porous Media* **6**, 407–433.

Bravo, M. C., Araujo, M. & Lago, M. E. 2007 Pore network modelling of two-phase flow in a liquid–(disconnected) gas system. *Physica* A **375**, 1–17.

Brooks, R. H. & Corey, A. T. 1964 Hydraulic properties of porous media. *Tech. Rep.* Hydrol. Paper 3. Colorado State University.

Brusseau, M. L., Peng, S., Schnaar, G. & Constanza-Robinson, M. S. 2006 Relationships among air–water interfacial area, capillary pressure, and water saturation for a sandy porous medium. *Water Resour. Res.* **42**, W03501.

Brusseau, M. L., Popovicova, J. & Silva, J. A. K. 1997 Characterizing gas–water interfacial and bulk-water partitioning for gas phase transport of organic contaminants in unsaturated porous media. *Environ. Sci. Technol.* **31**, 1645–1649.

Celia, M. A., Reeves, P. C. & Ferrand, L. A. 1995 Recent advances in pore scale models for multiphase flow in porous media. *Rev. Geophys.* **33** (S1), 1049–1058.

Chen, D. Q., Pyrak-Nolte, L. J., Griffin, J. & Giordano, N. J. 2007 Measurement of interfacial area per volume for drainage and imbibition. *Water Resour. Res.* **43**, W12504.

Chen, L. & Kibbey, T. C. G. 2006 Measurement of air–water interfacial area for multiple hysteretic drainage curves in an unsaturated fine sand. *Langmuir* **22**, 6874–6880.

Cheng, J. T., Pyrak-Nolte, L. J. & Nolte, D. D. 2004 Linking pressure and saturation through interfacial area in porous media. *Geophys. Res. Lett.* **31**, L08502.

Constantinides, G. N. & Payatakes, A. C. 1991 A theoretical model of collision and coalescence of ganglia in porous media. *J. Colloid Interface Sci.* **141**, 486–504.

Constantinides, G. N. & Payatakes, A. C. 1996 Network simulation of steady-state two-phase flow in consolidated porous media. *AIChE J.* **42**, 369–382.

Costanza-Robinson, M. S. & Brusseau, M. L. 2002 Air–water interfacial areas in unsaturated soils: evaluation of interfacial domains. *Water Resour. Res.* **38**, 13–1.

Culligan, K. A., Wildenschild, D., Christensen, B. S. B., Gray, W., Rivers, M. L. & Tompson, A. F. B. 2004 Interfacial area measurements for unsaturated flow through a porous medium. *Water Resour. Res.* **40**, W12413.

Culligan, K. A., Wildenschild, D., Christensen, B. S. B., Gray, W., Rivers, M. L. & Tompson, A. F. B. 2006 Pore-scale characteristics of multiphase flow in porous media: a comparison of air–water and oil–water experiments. *Adv. Water Resour.* **29**, 227–238.

Dahle, H. K. & Celia, M. A. 1999 A dynamic network model for two-phase immiscible flow. *Comput. Geosci.* **3**, 1–22.

Dahle, H. K., Celia, M. A. & Hassanizadeh, S. M. 2005 Bundle-of-tubes model for calculating dynamic effects in the capillary–pressure–saturation relationship. *Transport Porous Media* **58**, 5–22.

Das, D. B., Mirzaei, M. & Widdows, N. 2006 Non-uniqueness in capillary pressure–saturation–relative permeability relationships for two-phase flow in porous media: interplay between intensity and distribution of random micro-heterogeneities. *Chem. Engng Sci.* **61**, 6786–6803.

Dias, M. M. & Payatakes, A. C. 1986*a* Network models for two-phase flow in porous media. Part 1. Immiscible microdisplacement of non-wetting fluids. *J. Fluid Mech.* **164**, 305–336.

Dias, M. M. & Payatakes, A. C. 1986*b* Network models for two-phase flow in porous media. Part 2. Motion of oil ganglia. *J. Fluid Mech.* **164**, 337–358.

Fatt, I. 1956 The network model of porous media. Part I. Capillary pressure characteristics. *Petroleum Trans. AIME* **207**, 144–159.

Fayers, F. J., Blunt, M. J. & Christie, M. A. 1990 *Accurate Calibration of Empirical Viscous Fingering Models*. pp. 45–55. Technip.

Fong, K. W., Jefferson, T. H., Suyehiro, T. & Walton, L. 1993 *Guide to the SLATEC Common Mathematical Library*. Lawrence Livermore and Sandia National Laboratories, http://www.netlib.org/slatec/guide.

Gielen, T., Hassanizadeh, S. M., Leijnse, A. & Nordhaug, H. F. 2005 Dynamic effects in multiphase flow: a pore-scale network approach. In *Upscaling Multiphase Flow in Porous Media* (ed. D. B. Das & Hassanizadeh S. M.), pp. 217–236. Springer.

Hassanizadeh, S. M., Celia, M. A. & Dahle, H. K. 2002 Dynamic effects in the capillary pressure–saturation relationship and their impacts on unsaturated flow. *Vadose Zone J.* **1**, 38–57.

Hassanizadeh, S. M. & Gray, W. G. 1990 Mechanics and thermodynamics of multiphase flow in porous media including interphase boundaries. *Adv. Water Resour.* **13**, 169–186.

Hassanizadeh, S. M. & Gray, W. G. 1993*a* Thermodynamic basis of capillary pressure in porous media. *Water Resour. Res.* **29**, 3389–3405.

Hassanizadeh, S. M. & Gray, W. G. 1993*b* Toward an improved description of the physics of two-phase flow. *Adv. Water Resour.* **16**, 53–67.

Hassanizadeh, S. M., Oung, O. & Manthey, S. 2004 Laboratory experiments and simulations on the significance of non-equilibrium effect in the capillary pressure–saturation relationship. In *Unsaturated Soils: Experimental Studies. Proceedings of the International Conference: From Experimental Evidence towards Numerical Modelling of Unsaturated Soils* (ed. T. Schanz), vol. 1, pp. 3–14. Springer.

Held, R. J. & Celia, M. A. 2001 Modelling support of functional relationships between capillary pressure, saturation, interfacial area and common lines. *Adv. Water Resour.* **24**, 325–343.

Hughes, R. G. & Blunt, M. J. 2000 Pore scale modelling of rate effect in imbibition. *Transport Porous Media* **40**, 295–322.

Joekar-Niasar, V., Hassanizadeh, S. M. & Leijnse, A. 2008 Insights into the relationships among capillary pressure, saturation, interfacial area and relative permeability using pore-network modelling. *Transport Porous Media* **74** (2), 201–219.

Joekar-Niasar, V., Hassanizadeh, S. M., Pyrak-Nolte, L. J. & Berentsen, C. 2009 Simulating drainage and imbibition experiments in a high-porosity micromodel using an unstructured pore network model. *Water Resour. Res.* **45**, W02430.

Joekar-Niasar, V., Prodanović, M., Wildenschild, D. & Hassanizadeh, S. M. 2010 Network model investigation of interfacial area, capillary pressure and saturation relationships in granular porous media. *Water Resour. Res.* doi:10.1029/2009WR008585.

Kalaydjian, F. & Marle, C. M. 1987 Thermodynamic aspects of multiphase flow in porous media. *Collection Colloques et Séminaires – Institut Français du Pétrole* **45**, 513–531.

King, P. R. 1987 The fractal nature of viscous fingering in porous media. *J. Phys.* A **20**, L529–L534.

Knudsen, H. A., Aker, E. & Hansen, A. 2002 Bulk flow regimes and fractional flow in 2d porous media by numerical simulations. *Transport Porous Media* **47**, 99–121.

Knudsen, H. A. & Hansen, A. 2002 Relation between pressure and fractional flow in two-phase flow in porous media. *Phys. Rev.* E **65**, 056310-1–056310-10.

Koplik, J. & Lasseter, T. J. 1985 Two-phase flow in random network models of porous media. *Soc. Petrol. Engng J.* **25**, 89–110.

Koval, E. J. 1963 A method for predicting the performance of unstable miscible displacements in heterogenous media. *Trans. AIME* **219**, 145–150.

Ma, S., Mason, G. & Morrow, N. R. 1996 Effect of contact angle on drainage and imbibition in regular polygonal tubes. *Colloids Surfaces* **117**, 273–291.

Manthey, S., Hassanizadeh, S. M. & Helmig, R. 2005 Macro-scale dynamic effects in homogeneous and heterogeneous porous media. *Transport Porous Media* **58**, 121–145.

Mason, G. & Morrow, N. R. 1987 Meniscus configurations and curvatures in non-axisymmetric pores of open and closed uniform cross-section. *Proc. R. Soc. Lond.* A **414** (1846), 111–133.

Mayer, R. P. & Stowe, R. A. 1965 Mercury porosimetry-breakthrough pressure for penetration between packed spheres. *J. Colloid Sci.* **20**, 891–911.

Mirzaei, M. & Das, D. B. 2007 Dynamic effects in capillary pressure–saturations relationships for two-phase flow in 3d porous media: implications of micro-heterogeneities. *Chem. Engng Sci.* **62** (7), 1927–1947.

Mogensen, K. & Stenby, E. H. 1998 A dynamic two-phase pore-scale model for imbibition. *Transport Porous Media* **32**, 299–327.

Nguyen, V. H., Sheppard, A. P., Knackstedt, M. A. & Pinczewski, W. 2006 The effect of displacement rate on imbibition relative permeability and residual saturation. *J. Petrol. Sci. Engng* **52**, 54–70.

Niessner, J. & Hassanizadeh, S. M. 2008 A model for two-phase flow in porous media including fluid–fluid interfacial area. *Water Resour. Res.* **44**, W08439.

Nordbotten, J. M., Celia, M. A., Dahle, H. K. & Hassanizadeh, S. M. 2007 Interpretation of macroscale variables in Darcy's law. *Water Resour. Res.* **43** (8), W08430.

Nordbotten, J. M., Celia, M. A., Dahle, H. K. & Hassanizadeh, S. M. 2008 On the definition of macroscale pressure for multiphase flow in porous media. *Water Resour. Res.* **44** (6), W06S02.

Nordhaug, H. F., Celia, M. & Dahle, H. K. 2003 A pore network model for calculation of interfacial velocities. *Adv. Water Resour.* **26**, 1061–1074.

O'Carroll, D. M., Phelan, T. J. & Abriola, L. M. 2005 Exploring dynamic effects in capillary pressure in multistep outflow experiments. *Water Resour. Res.* **41**, W11419.

Oung, O., Hassanizadeh, S. M. & Bezuijen, A. 2005 Two-phase flow experiments in a geocentrifuge and the significance of dynamic capillary pressure effect. *J. Porous Media* **8**, 247–257.

Pan, C., Hilpert, M. & Miller, C. T. 2004 Lattice-Boltzmann simulation of two-phase flow in porous media. *Water Resour. Res.* **40**, W01501.

Payatakes, A. C. 1982 Dynamics of oil ganglia during immiscible displacement in water-wet porous media. *Annu. Rev. Fluid Mech.* **14**, 365–393.

Pereira, G. G., Pinczewski, W. V., Chan, D. Y. C., Paterson, L. & Øren, P. E. 1996 Pore-scale network model for drainage-dominated three-phase flow in porous media. *Transport Porous Media* **24**, 167–201.

Porter, M. L., Schaap, M. G. & Wildenschild, D. 2009 Lattice-Boltzmann simulations of the capillary pressure–saturation–interfacial area relationship for porous media. *Adv. Water Resour.* **32** (11), 1632–1640.

Prat, M. 2002 Recent advances in pore-scale models for drying of porous media. *Chem. Engng J.* **86**, 153–164.

Princen, H. M. J. 1969*a* Capillary phenomena in assemblies of parallel cylinders. Part I. Capillary rise between two cylinders. *Colloid Interface Sci.* **30**, 69–75.

Princen, H. M. J. 1969*b* Capillary phenomena in assemblies of parallel cylinders. Part II. Capillary rise in systems with more than two cylinders. *Colloid Interface Sci.* **30**, 359–371.

Princen, H. M. J. 1970 Capillary phenomena in assemblies of parallel cylinders. Part III. Liquid columns between horizontal parallel cylinders. *Colloid Interface Sci.* **34**, 171–184.

Pyrak-Nolte, L. J. 2007 Measurement of interfacial area per volume for drainage and imbibition. http://www.physics.purdue.edu/rockphys/DataImages/index.php.

Ransohoff, T. C. & Radke, C. J. 1988 Laminar flow of a wetting liquid along the corners of a predominantly gas-occupied noncircular pore. *J. Colloid Interface Sci.* **121**, 392–401.

Reeves, P. C. & Celia, M. A. 1996 A functional relationship between capillary pressure, saturation, and interfacial area as revealed by a pore-scale network model. *Water Resour. Res.* **32**, 2345–2358.

Singh, M. & Mohanty, K. K. 2003 Dynamic modelling of drainage through three-dimensional porous materials. *Chem. Engng Sci.* **58**, 1–18.

Stauffer, F. 1978 Time dependence of the relations between capillary pressure, water content and conductivity during drainage of porous media. In *IAHR Symposium on Scale Effects in Porous Media*, Thessaloniki, Greece, pp. 3.35–3.52.

Thompson, K. E. 2002 Pore-scale modelling of fluid transport in disordered fibrous materials. *AIChE J.* **48**, 1369–1389.

Valvanides, M. S., Constantinides, G. N. & Payatakes, A. C. 1998 Mechanistic model of steady-state two-phase flow in porous media based on ganglion dynamics. *Transport Porous Media* **30**, 267–299.

Valvatne, P. H. & Blunt, M. J. 2004 Predictive pore-scale modelling of two-phase flow in mixed wet media. *Water Resour. Res.* **40**, W07406.

Van der Marck, S. C., Matsuura, T. & Glas, J. 1997 Viscous and capillary pressures during drainage: network simulations and experiments. *Phys. Rev.* E **56**, 5675–5687.

Vidales, A. M., Riccardo, J. L. & Zgrabli, G. 1998 Pore-level modelling of wetting on correlated porous media. *J. Phys.* D*, Appl. Phys.* **31**, 2861–2868.

Washburn, E. W. 1921 The dynamics of capillary flow. *Phys. Rev.* **17**, 273–283.

Whitaker, S. 1977 Simultaneous heat, mass, and momentum transfer in porous media: a theory of drying. *Adv. Heat Transfer* **13**, 119–200.

Zhou, D., Blunt, M. J. & Orr, F. M. 1997 Hydrocarbon drainage along corners of noncircular capillaries. *J. Colloid Interface Sci.* **187**, 11–21.